Arab J Geosci (2016) 9:755
DOI 10.1007/s12517-016-2775-1

ORIGINAL PAPER

Chemostratigraphy of the Cenomanian-Turonian shallow-water carbonate: new correlation for the rudist levels from north Sinai, Egypt

Yasser F Salama[1,2] · **Gouda I Abdel-Gawad**[1] · **Shaban G Saber**[1] · **Soheir H El-Shazly**[1] · **G. Michael Grammer**[2] · **Sacit Özer**[3]

Received: 19 December 2015 / Accepted: 29 November 2016

Abstract The present study aims to provide carbon-isotope curves for the Cenomanian to Turonian rudist-dominated successions in north Sinai. The high-resolution carbon-isotope curves obtained from north Sinai sections provide new insight for calibrating the age of rudists as well as for evaluating the effects of the oceanic anoxic event 2 (OAE2) on rudist communities. The primary goals are (1) to provide a high-resolution sequence stratigraphic framework for the Cenomanian-Turonian succession, (2) to use rudist and ammonite biostratigraphic data to distinguish the stratigraphic levels of the rudist species, and (3) to integrate the chemostratigraphic ($\delta^{13}C$) profile and the rudist levels to improve the biostratigraphy based on the rudist distributions and the carbon-isotope data. The recognition of three ammonite zones through the Cenomanian-Turonian succession was utilized to identify four temporally significant rudist levels indicative of the Lower Cenomanian, Middle Cenomanian, Upper Cenomanian, and Middle Turonian, respectively. Most of the rudists occur in the highstand deposits of medium-scale sequences. Carbon- and oxygen-isotopic analyses were carried out on both rudists and surrounding carbonate units. Based on the variations in the carbon-isotope signals, 12 chronostratigraphic segments were identified in the studied sections. The Cenomanian carbon-isotope segments (C23–C30) were obtained from the Halal Formation at Gabal Yelleg and Gabal Maaza sections, while the Turonian segments (C30–C34) were measured from the Wata Formation at Gabal Yelleg section. The carbon-isotope record from the studied sections is consistent with the trends documented in previous studies of the Tethyan realm. The Cenomanian-Turonian boundary is placed at the onset of falling carbon-isotope values ($\delta^{13}C$) from 2.61 to −0.25‰ in the upper part of OAE2 with the carbon-isotope segment C30 at Gabal Yelleg. The negative shift in $\delta^{13}C$ values (C33) occurred in the Middle Turonian lowstand deposits characterizing the global sea level fall during this interval.

Keywords Cenomanian-Turonian carbonate · North Sinai · Chemostratigraphy

Introduction

Various species of rudists are widespread in the Aptian to Turonian successions in north Egypt (De Castro and Sirna 1996; Steuber and Bachmann 2002; Aly et al. 2005; El-Hedeny 2007; Saber et al. 2009; Abdel-Gawad et al. 2011; El-Shazly et al. 2011) and the Arabian platform (van Buchem et al. 1996, 2002, 2010, 2011; Al-Ghamdi and Read 2010; Droste 2010; Yose et al. 2010; Strohmenger et al. 2010; Razin et al. 2010; Moosavizadeh et al. 2015). During the Aptian to Albian, the Tethys transgression inundated the northernmost part of Sinai, resulting in the deposition of shallow-water, rudist-dominated sediments (Kuss and Bachmann 1996; Bachmann et al. 2010). In the Cenomanian-Turonian

Electronic supplementary material The online version of this article (doi:10.1007/s12517-016-2775-1) contains supplementary material, which is available to authorized users.

✉ Yasser F Salama
yasser.salama@science.bsu.edu.eg

[1] Geology Department, Faculty of Sciences, Beni-Suef University, Bani Suef, Egypt

[2] Boone Pickens School of Geology, Noble Research Center, Oklahoma State University, Stillwater, USA

[3] Mühendislik Fakültesi, Dokuz Eylül Üniversitesi, Izmir, Turkey

Published online: 17 December 2016

interval, the carbonate platform extended southward in Egypt, and rudists were deposited in the north Western Desert and on the western side of the Gulf of Suez (De Castro and Sirna 1996; El-Hedeny and El-Sabbagh 2005; Abdel-Gawad et al. 2011; Saber 2012). In addition, local environmental parameters such as rate of sedimentation and accommodation space controlled variations in the rudist distribution in the transgressive and highstand system tracts of the Cretaceous carbonate platform (Schulze et al. 2003; Bauer et al. 2004; Bover-Arnal et al. 2009; Saber et al. 2009; Droste 2010). Because of the wide distribution and variation of rudist species, they are especially appropriate for evaluating the marine isotopic composition during this time period in Egypt.

Variation in the stable carbon-isotope ratio ($\delta^{13}C$) allowed most stratigraphic studies to use the $\delta^{13}C$ values obtained from the marine Cretaceous successions for global stratigraphic correlation (Jarvis et al. 2006; Voigt et al. 2007; Embry et al. 2010; Vincent et al. 2010; Gale et al. 2011; Ghanem et al. 2012; Frijia et al. 2015; Huck and Heimhofer 2015). The analysis of the oceanic anoxic event 2 (OAE2) has been used primarily as a global chemostratigraphic marker. Moreover, the origin of the OAE2 at the Cenomanian-Turonian (C-T) boundary has been the recent focus of several studies (Turgeon and Creaser 2008; Gebhardt et al. 2010; Batenburg et al. 2016; Wohlwend et al. 2015; Dickson et al. 2016; Gambacorta et al. 2016; Jenkyns et al. 2016; Wendler et al. 2016; Zheng et al. 2016). An increase in the rate of organic-carbon burial during OAE2 was interpreted as a result of (1) sea level transgression (Keller and Pardo 2004), (2) volcanic events (Zheng et al. 2013, 2016; Jenkyns et al. 2016), and (3) an acceleration in the hydrological cycle. Such hydrologic changes affected the nutrient supply and stratification of the sediments (Van Helmond et al. 2014; Wendler et al. 2016). In addition to a positive $\delta^{13}C$ excursion that marked the onset of OAE2, the significant biological changes across the Cenomanian-Turonian transition are also a valuable tool to trace this event (Gebhardt et al. 2010; Elderbak et al. 2014; Reolid et al. 2015). The species extinctions and diversifications at the C-T boundary are related to the major rise of sea level and an increase in the rates of productivity (Keller and Pardo 2004). As an example, the numbers and size of benthic foraminifera have been shown to document the change from oxic to dysoxic conditions during OAE2 (Gebhardt et al. 2010). Therefore, changes in the benthic foraminiferal diversities within the OAE2 interval should be indicative of variations in bottom water oxygenation and the organic matter flux (Friedrich et al. 2006). Likewise, the OAE2 event has been considered as one of the major causal mechanisms for the rudistid extinction around the C-T boundary, one that can be related to increased productivity and the eutrophic conditions (Kauffman 1995; Lebedel et al. 2015). In Egypt, most of the previous studies utilizing carbon isotopes have been focused on OAE2 as a global chronostratigraphic marker at the C-T boundary (Shahin 2007; Gertsch et al. 2010; El-Sabbagh et al. 2011; Nagm et al. 2014).

To date, no study has introduced a complete carbon-isotope profile for the Cenomanian-Turonian successions in Sinai. One of the main goals of the present study is the measurement of the carbon ($\delta^{13}C$) and oxygen ($\delta^{18}O$) isotope compositions of both rudist shells and bulk carbonate of the Cenomanian-Turonian successions at north Sinai. The isotope data has been investigated in order to understand whether the isotopic signatures reflect primary environmental signals or diagenetic effects and affect of freshwater interaction. Moreover, the first continuous high-resolution carbon-isotope profile for the Cenomanian-Turonian interval is presented in this work. The calibration of the $\delta^{13}C$-isotope profile with the biostratigraphy data enables us to correlate the present isotope data with the published coeval isotope records of the adjacent Tethyan carbonates. This correlation provides a higher accuracy age dating of the rudist levels and the Cenomanian-Turonian sequences in north Sinai. Also, this work highlights a link between the distribution of rudists and the trophic conditions, as well as the depositional system tracts.

Regional context

The study area lies in the northern part of Sinai (Fig. 1). The studied sections are part of the Syrian arc system tectonic domain, which is one of the distinctive structural features in the unstable shelf in Egypt. Gabal Maaza is located along the eastern limb of Gabal Maghara, with Gabal Yelleg situated approximately 25 km southeast of Gabal Maghara.

The Cenomanian-Turonian successions in Egypt are mostly characterized by rudist-dominated strata (Parnes 1987; Bauer et al. 2004; El-Hedeny and El-Sabbagh 2005; El-Hedeny 2007; Saber et al. 2009; Zakhera 2010; Hamama 2010; Abdel-Gawad et al. 2011). In Sinai, many authors have used the Halal Formation to describe the complete Cenomanian successions (Abdallah et al. 1996; Lüning et al. 1998; Aly et al. 2005; Saber et al. 2009), while other workers have assigned an Albian-Cenomanian age to the Halal Formation (Bachmann et al. 2003; El-Qot et al. 2009). To the south, the Halal Formation is replaced by the siliciclastic Raha Formation (Fig. 1) and used to designate the marine Cenomanian deposits in central and south Sinai (Shahin and Kora 1991; Kora and Genedi 1995; Bauer et al. 2001; Saber 2002; Abdel-Gawad et al. 2004; Gertsch et al. 2010). The Raha Formation overlies the Lower Cretaceous fluvial Malha Formation and reflects the first marine transgression during the Cenomanian in south Sinai.

The Turonian rocks that are exposed in Sinai conformably overlie the Cenomanian successions (Fig. 1). In west central Sinai and the Gulf of Suez region, the Turonian succession is represented by Abu Qada (siliciclastics and carbonates) and Wata (carbonates) Formations (Ghorab 1961; El-Shinnawi

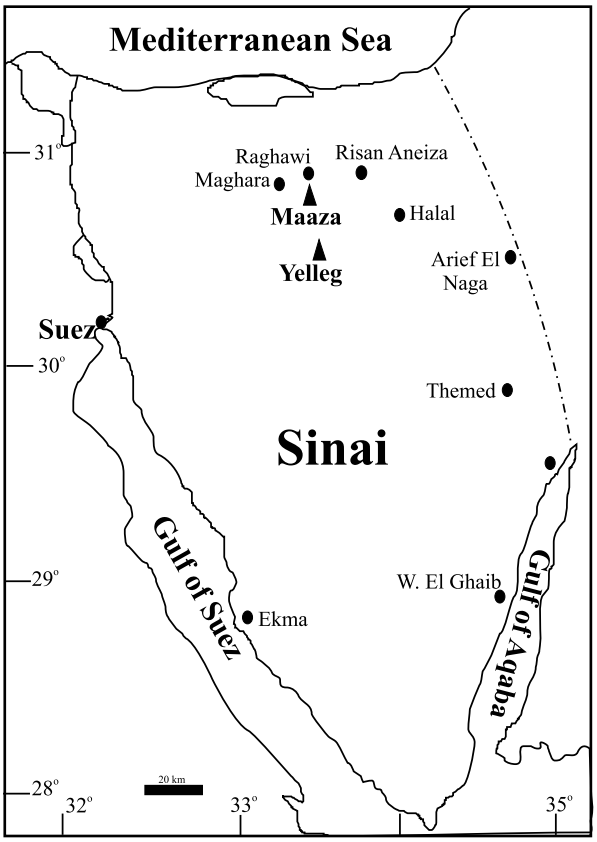

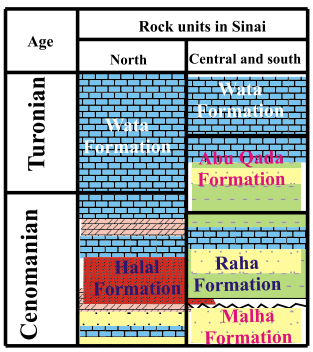

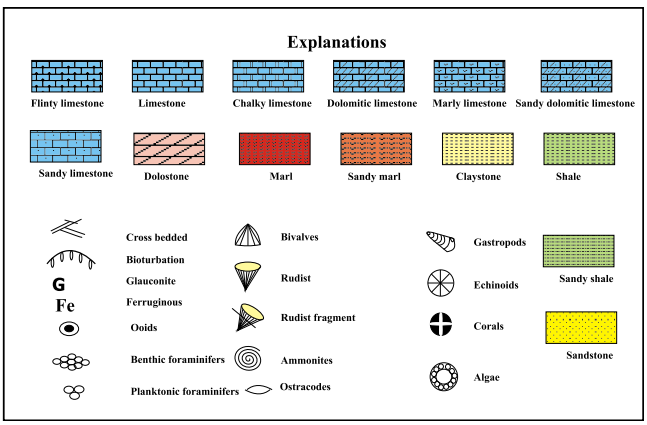

Fig. 1 Location map for the studied sections (*triangles*) in north Sinai. On the *left side* (*bottom*), the Cenomanian-Turonian rock units in Sinai; Malha Formation is fluvial facies, Raha Formation is marine siliciclastics, Halal Formation is marine carbonate, Abu Qada Formation is marine siliciclastics, and Wata is marine carbonate

and Sultan 1973; Kora and Genedi 1995; Shahin 2007; El-Qot et al. 2009; Gertsch et al. 2010). In some publications, the lower boundary of Abu Qada Formation is defined as of Late Cenomanian (Gertsch et al. 2010). In addition, the scarcity of siliciclastic materials in north Sinai encouraged some authors (Abdel-Gawad and Zalat 1992; Hassan et al. 1992; Ziko et al. 1993) to interpret the Wata Formation as representing the entire Turonian succession.

The Cenomanian Halal Formation is completely recorded at Gabal Yelleg and Gabal Maaza (Fig. 2). The Cenomanian deposits consist of an alternation of limestone, rudist-bearing limestone, dolostone, and marl. The abundance of rudists, oysters, gastropods, calcareous algae, and benthic foraminifera within these deposits indicates shallow-marine conditions. The Turonian Wata Formation conformably overlies the Cenomanian deposits with a marker ammonite bed at the contact (Fig. 2). The Turonian succession at Gabal Yelleg attains a thickness of about 110 m. The lower part of this rock unit at Gabal Yelleg is characterized by chalky, oolitic, thick-bedded, and fossiliferous limestone. Ammonites observed at the base include *Choffaticeras segne* and *Thomasites rollandi*.

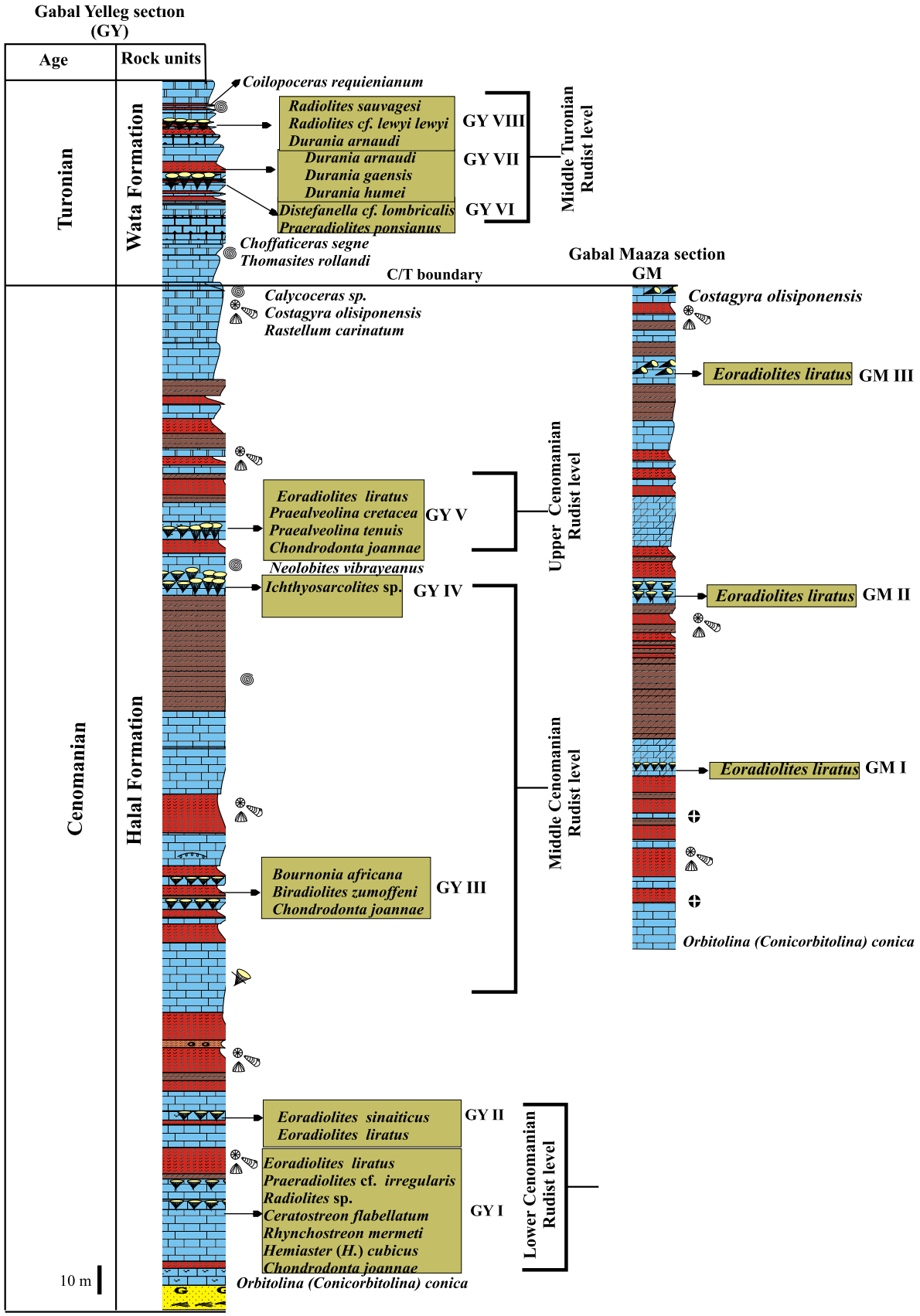

Fig. 2 Cenomanian-Turonian stratigraphic sections with rudist levels and sublevels. *GY* Gabal Yelleg, *GM* Gabal Maaza

Methods

Two sections were described and measured from the Cenomanian-Turonian successions in north Sinai. The rudist specimens and other associated fauna have been collected and identified from the studied sections. In addition, rock samples were collected for thin sections. To construct the sequence stratigraphic framework, most of the sequence boundaries and exposure surfaces were identified in the field. These observations were complemented with the study of the thin sections for textural description and identification of the bioclastic components. The previously established sequence stratigraphic framework and accompanying rudist data documented by Saber et al. (2009) helped in recognizing the age of the rudists as well as the correlation of the rudist levels with the different system tracts. However, in order to subdivide the third sequences into high-frequency, fourth-order sequences, additional facies analysis and field data were used in this study.

Samples for carbon ($\delta^{13}C$) and oxygen ($\delta^{18}O$) isotope analyses were collected at 1–5-m intervals from the exposed sections at Gabal Yelleg and Maaza in north Sinai. A total of 165 bulk carbonate and rudist samples were used for the analysis. The samples were selected as follow: 107 samples from the Cenomanian Halal Formation at Gabal Yelleg and Maaza sections and 31 samples from the Turonian Wata Formation at Gabal Yelleg. The samples are mainly bioclastic and dolomitic limestone at Gabal Maaza. However, at Gabal Yelleg, the samples are bioclastic wackestones and packstones and rudist bafflestone. In the rudist-bearing intervals, 27 samples were collected from the outer layers of the well-preserved rudist shells. The stable isotope analyses were performed at the Stable Isotope Laboratory in the University of Miami, USA, using standard methods as detailed in Swart and Melim (2000), Swart and Eberli (2005), and Swart et al. (2005). The carbonate samples were digested in 100% H_3PO_4 at 90 °C using a common acid bath. The liberated CO_2 was analyzed for oxygen and carbon isotopes on a Finnigan MAT 251 mass spectrometer. Data have been corrected for unusual interferences and are reported in standard δ notation on the VPDB scale. The overall precision of this method is better than 0.08‰. The $\delta^{13}C$ and $\delta^{18}O$ results are shown in Tables 1, 2, 3, and 4 at Electronic Supplementary Material ESM_1.pdf.

Finally, the integration of the carbon-isotope profile, the rudist levels, and the existing biostratigraphic data provide a workable stratigraphic scheme for the Cenomanian-Turonian successions.

Stratigraphy of the rudists

The biostratigraphy based on rudists has been used by many authors (Vicens et al. 1998; Sari and Özer 2009; Scott 2010; Özer and Ahmad 2015). The long ranges of some rudist species, however, influence the efficacy of the rudists for biostratigraphic applications. The presence of additional high-resolution biostratigraphic data such as with ammonite zonation have been shown to provide a precise biostratigraphy for the rudist-bearing successions in the Tethyan realms (Simone et al. 2003; Sari et al. 2004). The Cenomanian-Turonian rudist horizons at Gabal Yelleg were subdivided into nine rudist assemblages in Saber et al. (2009). However, the precise age of these assemblages is controversial. In this work, utilization of the ammonite zones along with the global correlation of the $\delta^{13}C$ records allowed us to refine the stratigraphic position of these rudists (Fig. 2).

Based on the presence of ammonites, three zones are identified at Gabal Yelleg from older to younger; *Neolobites vibrayeanus* zone (Late Cenomanian), *C. segne-T. rollandi* zone (Early Turonian), and *Coilopoceras requienianum* zone (early Late Turonian). The ammonite zones provided a means to distinguish the rudist-bearing strata into four main rudist levels at Gabal Yelleg (Figs. 2 and 3a–h and Table 5 in ESM_1.pdf).

Lower Cenomanian rudist level

This rudist level was documented in the first 80 m from the base of Gabal Yelleg section above the occurrence of *Orbitolina* (*C*) *conica*. The rudist sublevel GY I is dominated by *Eoradiolites liratus*, *Praeradiolites* cf. *irregularis* (Fig. 3g), and *Radiolites* sp., and rudist sublevel GY II is characterized by an association of *Eoradiolites sinaiticus* and *E. liratus* (Fig. 3b, d). The first appearance of *O.* (*C*) *conica* below these rudist sublevels marks the Albian-Cenomanian boundary in Tethys (Schroeder and Neumann 1985).

Middle Cenomanian rudist level

This rudist level is recorded below the early Late Cenomanian *N. vibrayeanus*, and it is subdivided into two sublevels. The rudist sublevel GY III is represented by *Biradiolites zumoffeni* and *Bournonia africana* (Fig. 3a, f) that alternate with *Chondrodonta* beds. The rudist sublevel IV is dominated with *Ichthyosarcolites* sp.

Upper Cenomanian rudist level

This rudist level GY V contains *E. liratus* and *Chondrodonta joannae*. It is recorded above the Late Cenomanian *N. vibrayeanus* zone.

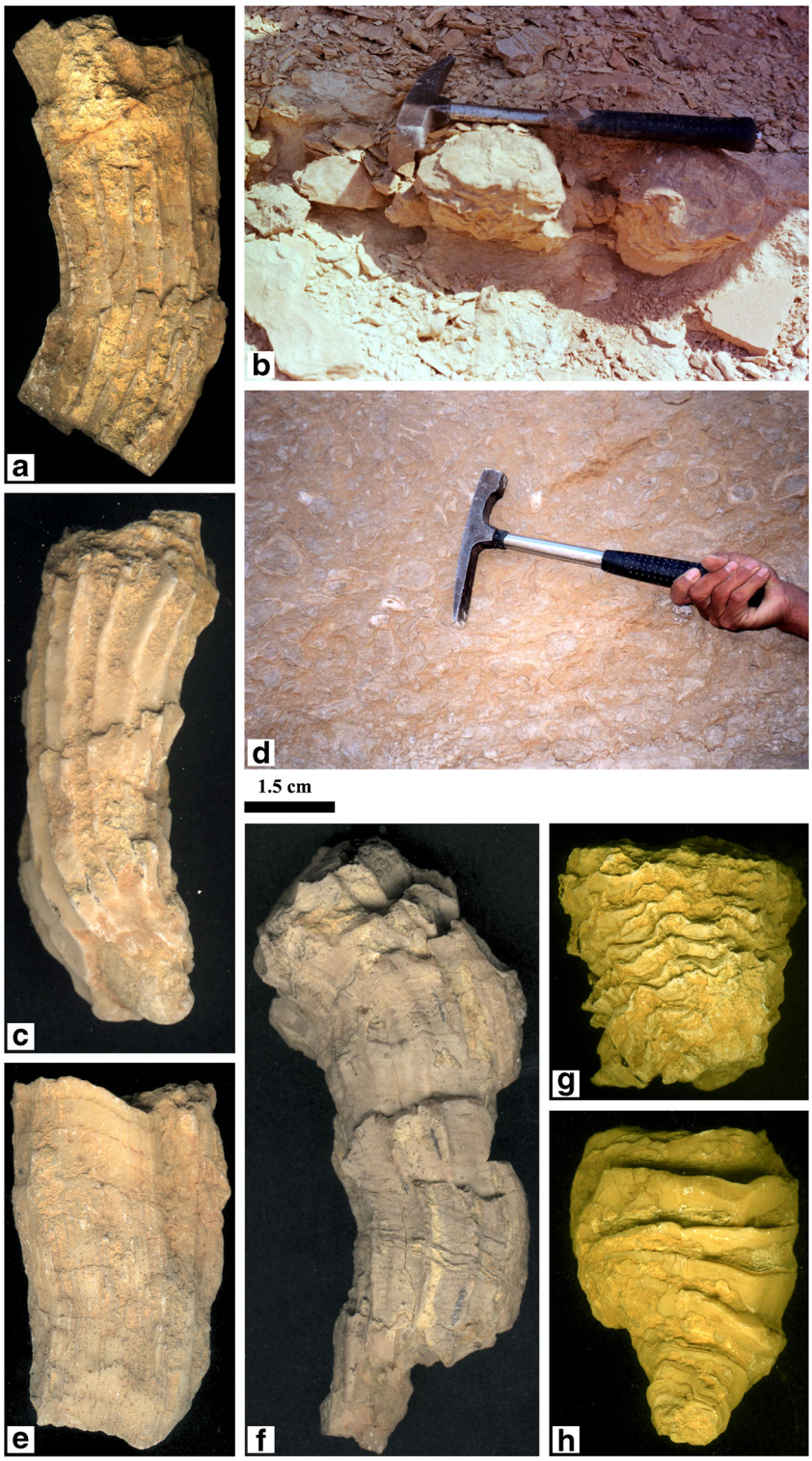

Fig. 3 **a** *Biradiolites zumoffeni* in rudist level GY III, Cenomanian, Halal Formation Gabal Yelleg. **b** Field photograph for *Eoradiolites sinaiticus* in vertical life position, Cenomanian, Halal Formation Gabal Yelleg. **c** *Distefanella* cf. *lombricalis*, Turonian Wata Formation, Gabal Yelleg. **d** Field photograph shows the bedding plane view for *Eoradiolites liratus*, Cenomanian, Halal Formation Gabal Yelleg. **e** *Durania arnaudi* Turonian Wata Formation, Gabal Yelleg. **f** *Bournonia africana* Cenomanian, Halal Formation Gabal Yelleg. **g** *Praeradiolites* cf. *irregularis*, Cenomanian, Halal Formation Gabal Yelleg. **h** *Praeradiolites ponsianus*, Turonian Wata Formation, Gabal Yelleg

Middle Turonian rudist level

This level includes the first Turonian rudist species that flourished the carbonate platform after the OAE2 at Gabal Yelleg. Three rudist sublevels GY VI–VIII are identified in the interval between *C. segne-T. rollandi* zone (Early Turonian) and *C. requienianum* zone (early Late Turonian). Accordingly, a precise age of these rudist sublevels GY VI–VIII is of Middle Turonian. The identified Turonian rudist species are *Radiolites sauvagesi*, *Radiolites* cf. *lewyi lewyi*,

Distefanella lombricalis (Fig. 3c), *Durania gaensis*, *Durania arnaudi* (Fig. 3e), *Durania humei*, and *Praeradiolites ponsianus* (Fig. 3h).

At Gabal Maaza of north Sinai, the rudist levels are difficult to access, but abundant rudist fragments have been observed in many limestone beds. Three rudist levels GM I, GM II, and GM III with reworked *E. liratus* have been noted.

Rudist facies and system tracts

The rudist-bearing beds at Gabal Yelleg are mainly bafflestone, floatstone, wackestone, and rudstone microfacies with rudists, benthic foraminifera, and *Chondrodonta* (Fig. 4). These facies are developed in the transgressive and the highstand system tracts of the depositional sequences. Moreover, the Cenomanian-Turonian successions contain the high-energy, shallow-marine bioclastic grainstone and rudstone. The facies is intercalated with fossiliferous wackestone and marl with oysters, gastropods, and ammonites. The rudist-bearing beds at Gabal Maaza are mainly floatstone and rudstone intercalated with dolostone and highly dolomitized limestones. The microfacies investigations as well as the depositional environment and the sequence boundaries within the Cenomanian-Turonian units allowed for the identification of five third-order depositional sequences. These sequences were deposited on a carbonate ramp (Fig. 5). The temporal subdivision of the sequences follows the time duration as proposed by Vail et al. (1991) and Haq et al. (1988) into third-order (0.5–3 my) and fourth-order sequences (0.5–0.08 my). In this study, the third-order depositional sequences (third order) of Saber et al. (2009) are subdivided into nine medium-scale (fourth order) sequences based on the field observation and the vertical facies change (Figs. 6, 7, and 8 at Electronic Supplementary Material ESM_2.pdf).

Sequence 1 (Lower-Middle Cenomanian)

Sequence 1 (third order) is composed of three medium-scale sequences (fourth order) and is overall more condensed at the Gabal Maaza location than at Gabal Yelleg. The sequence boundary (SB1) is marked by a thin, ferruginous hard crust with plant remains and iron concretions at Gabal Yelleg and is characterized by intensive meteoric diagenesis including

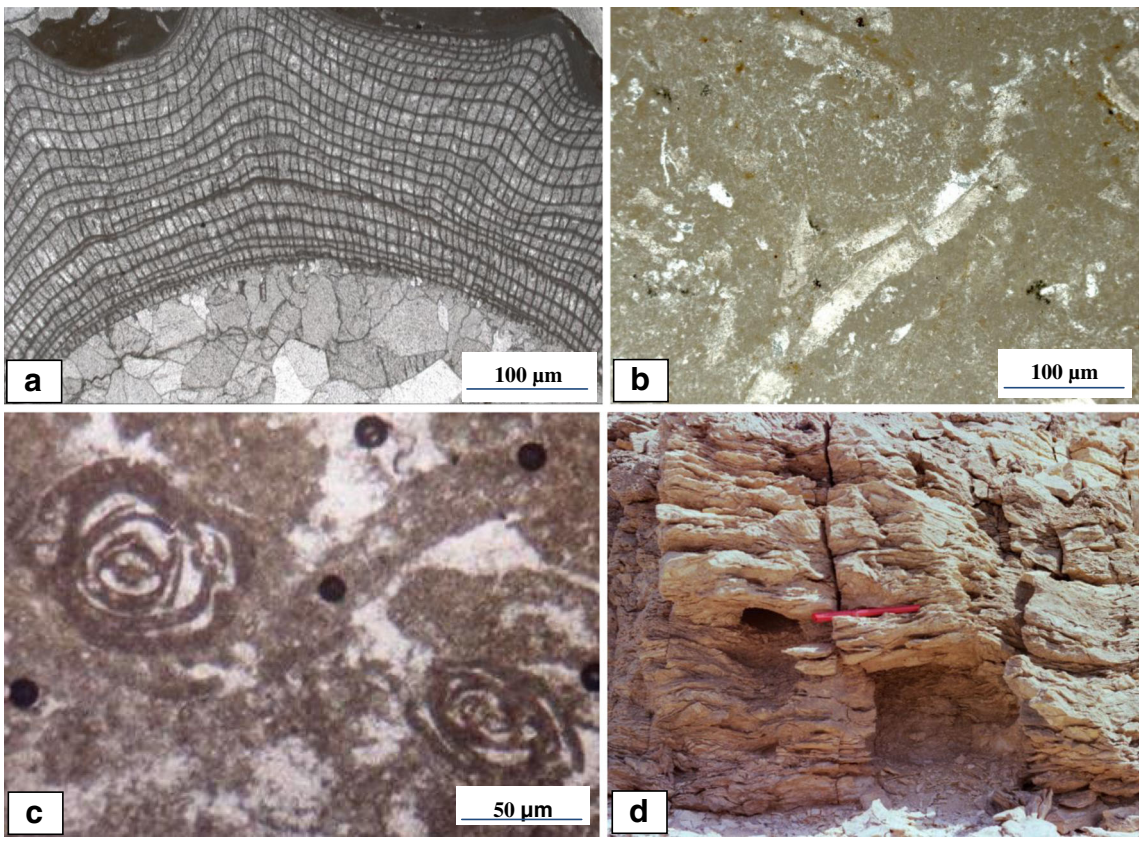

Fig. 4 Rudist-bearing beds. **a** Rudist bafflestone; cross section shows the cellular structure of the outer layer in *Bournonia* sp., the inner layer replaced by blocky calcite crystals, Cenomanian, Yelleg section. **b** Rudist floatstone; note that the presence of rudist fragments flow in micrite, Turonian, Yelleg section. **c** Benthic foraminifer wackestone with miliolids, Cenomanian, Yelleg section. **d** *Chondrodonta* bed, micritic limestone with tightly packed shells of chondrodontid bivalves, Cenomanian, Gabal Yelleg

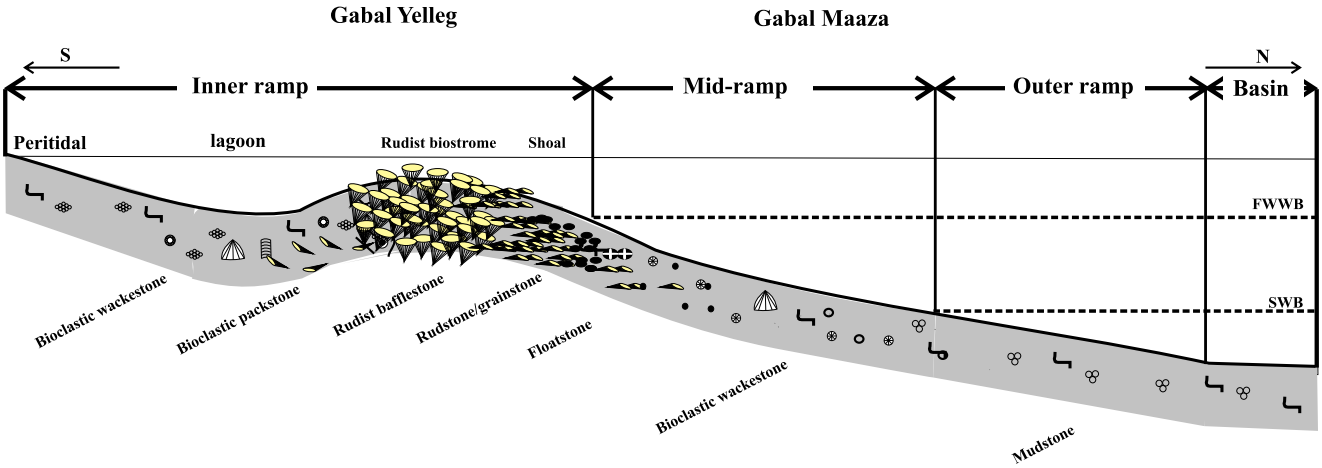

Fig. 5 Depositional model with different microfacies for the Cenomanian-Turonian successions in north Sinai. The rudist biostrome is the main element of the carbonate ramp thrived in the shallow part and pass laterally to deep facies with rudist debris, planktonic foraminifers, and echinoids in the outer ramp. The shallower inner ramp contains wackestone and packstone with benthic foraminifer mollusks and calcareous algae

dissolution, dolomitization, and dedolomitization at Gabal Maaza. Moreover, this sequence boundary exhibits a negative shift (depletion) in both $\delta^{13}C$ and $\delta^{18}O$ at Gabal Maaza.

Four rudist sublevels occur within the highstand system tracts of the medium-scale (fourth order) sequences at Gabal Yelleg. The rudists are in life position forming bafflestone and floatstone facies. At Gabal Maaza, the rudists are fragmented and displaced from life position forming rudstone and floatstone facies.

At Gabal Yelleg, the lowstand system tracts are characterized by subtidal bars that consist of cross-bedded sandstones with minor mudstone deposited on associated mudflats. Corresponding LST deposits are not recorded at Gabal Maaza. The transgressive system tract at Gabal Yelleg is represented by two medium-scale (fourth order) sequences. The first one (early transgressive system tract of sequence 1) is characterized by high-energy shoals at the base, followed by shallow subtidal rudist-dominated bafflestone/floatstone (rudist sublevels GY I and II) and bioclastic wackestones with abundant benthic foraminifera (Figs. 6 and 9 at ESM_2.pdf). The second medium-scale (fourth order) sequence at Gabal Yelleg is interpreted as late transgressive system tract deposits. These are composed of shallow subtidal and open lagoon facies, including bioclastic and peloidal wackestone with abundant of benthic foraminifera, ostracodes, bivalves, gastropods, and echinoids. This is followed by rudist bafflestone (rudist sublevel GY III) and bioclastic wackestone with *Praealveolina* sp. at the top.

The transgressive system tract at Gabal Maaza is composed of two medium-scale sequences (fourth order). The first medium-scale sequence is represented by the early transgressive system tract of the third-order sequence 1. It consists mainly of fossiliferous marl intercalated with high-energy oolitic grainstone shoals and bioclastic rudstones (Figs. 7 and 9 at ESM_2.pdf). The second medium-scale sequence consists of deeper subtidal wackestone and marl with planktic foraminifera. This is followed by shallow-marine platform deposits consisting of dolostone, rudist rudstone, mudstone, and wackestone with benthic foraminifera, bivalves, and gastropods.

The highstand system tracts of sequence 1 in both sections (Gabal Yelleg and Maaza) are dominated by dolostone facies. These highstand system tract deposits of sequence 1 (third order) form one medium-scale sequence (Figs. 6, 7, and 9 at ESM_2.pdf). At Gabal Yelleg, the highstand deposits initiated with slightly deeper subtidal facies of marl and mudstone comprised of echinoids and planktic foraminifera. These deposits are followed by dolostone, rudist bafflestone (rudist sublevel GY IV), and bioclastic wackestones, which are deposited in the shallow subtidal zone (Fig. 9 at ESM_2.pdf). The highstand deposits are capped with a brecciated hardground that is ferruginous and contains a thin iron crust. At Gabal Maaza, the highstand deposits consist mainly of dolostone with thin beds of marl, fragmented rudist-bearing limestone, and mudstone intercalations.

The third-order sequence 1 is correlated with the Early–earliest Middle Cenomanian sequence (MFS K120) of the Arabian Plate (van Buchem et al. 2011).

Sequence 2 (Middle-Upper Cenomanian)

Sequence 2 (third order) is delineated at the base by the Middle-Upper Cenomanian boundary where it is overlain by *N. vibrayeanus* of the early Late Cenomanian age (Abdallah et al. 2001; Kassab and Obaidalla 2001; Saber et al. 2009).

The sequence boundary is marked by a hardground that is characterized by dedolomitization and the presence of ferruginous and iron crusts at Gabal Yelleg. Because ammonite

biostratigraphy was not available at Gabal Maaza, carbon isotopes were used to correlate SB2 from Gabal Yelleg to Gabal Maaza. This sequence boundary is characterized by a pronounced negative shift in $\delta^{13}C$ and $\delta^{18}O$ values (carbon-isotope segment C27).

At Gabal Yelleg, the transgressive system tract of sequence 2 (third order) corresponds to the medium-scale sequence 4 (fourth order) and begins with outer ramp marls rich in ammonites passing upward into shallow subtidal rudist floatstone (rudist sublevel GY V), bioclastic wackestone, dolostone, and algal grainstone (Figs. 6 and 10 at ESM_2.pdf). At Gabal Maaza, the transgressive system tract (TST) deposits are also represented by medium-scale sequence 4 that consists mainly of mudstone, rudist floatstone, and marl intercalations with planktic foraminifera at the base (Figs. 7 and 10 at ESM_2.pdf).

The highstand system tracts of sequence 2 (third order) at both locations are composed of packstones or mudstones near the base, followed by thick dolostone facies. This facies succession indicates the change from shallow subtidal and open lagoon to the lower intertidal facies of restricted circulation. These deposits form the medium-scale sequence 5 (fourth order) at Gabal Yelleg and Gabal Maaza (Figs. 6, 7, and 10 at ESM_2.pdf).

This third-order sequence 2 is well correlated with the Middle-Late Cenomanian sequence III of Iran (Razin et al. 2010) and corresponds to the Middle Cenomanian sequence (MFS K130) of the Arabian Plate (van Buchem et al. 2011).

Sequence 3 (Upper Cenomanian-Lower Turonian)

This third-order sequence is 45 m thick at the upper part of the Cenomanian Halal Formation and the lower part of the Turonian Wata Formation at Gabal Yelleg (Fig. 8 at ESM_2.pdf). Rudists were not observed nor have they been previously reported from this sequence. The absence of rudists may correspond to the mass extinction interval around the Cenomanian-Turonian boundary (Philip and Airaud-Crumiere 1991).

The transgressive system tract of sequence 3 began with outer ramp bioclastic wackestone and packstone deposits rich in echinoids, ammonites, and planktic foraminifera. This transgressive interval is globally synchronous and includes OAE2. The highstand system tract of sequence 3 is characterized by high-energy shallow subtidal deposits that consist of peloidal packstones, oolitic grainstones, and bioclastic rudstones. These deposits stabilized the Turonian carbonate platform prior to the deposition of the first Turonian rudists in the next sequence (third-order sequence 4; see Figs. 8 and 11 at ESM_2.pdf).

Sequence 3 corresponds to the Late Cenomanian-earliest Turonian sequence of the Arabian plate (van Buchem et al. 2011) and sequence IV of Iran (Razin et al. 2010).

Sequence 4 (Middle Turonian)

Sequence 4 is 28 m thick and recorded the middle part of the Wata Formation at Gabal Yelleg (Fig. 8 at ESM_2.pdf). Sequence boundary 4 coincides with a negative shift in $\delta^{13}C$ and $\delta^{18}O$ that may indicate an exposure surface. This sequence is subdivided into two fourth-order, medium-scale sequences (6 and 7). Two rudist sublevels are observed with the first appearance of genus *Durania* in this sequence (Fig. 8 at ESM_2.pdf).

The marl and bioclastic wackestone deposits with echinoids and planktic foraminifera form the transgressive system tract of sequence 4 (Figs. 8 and 11 at ESM_2.pdf). The early highstand system tract of this sequence is distinguished by the development of prograding platform. It is dominated by rudist bafflestones (rudist sublevels GY VI and VII) and marl containing open marine fauna (Figs. 8 and 11 at ESM_2.pdf).

Sequence 5 (Middle-Upper Turonian)

This sequence is expressed in the upper part of the Turonian Wata Formation at Gabal Yelleg. It is 55 m thick and composed mainly of marl and limestone with the latest rudist sublevels in the Wata Formation.

The presence of mudstones rich in ostracodes reflects deposition in restricted lagoon environments at the lowstand system tract of sequence 5 (Fig. 8 at ESM_2.pdf). The TST consists of quiet, deepwater subtidal facies of bioclastic mudstone/wackestone and marl. These facies contain deep marine fauna such as echinoids, ammonites, and planktic foraminifera. The shallow subtidal facies in the form of rudist bafflestones (rudist sublevel GY VIII) are observed in this TST. The highstand system tract deposits of sequence 5 consist of subtidal bioclastic packstone shoal facies and restricted lagoon wackestone. The topmost part of this system tract is a lime mudstone that is interpreted to have been deposited in a lower intertidal zone (Fig. 8 at ESM_2.pdf).

Stable isotope results

The ability of the rudists to preserve the oxygen- and carbon-isotope signatures of the Cretaceous shallow-marine carbonate platform has been supported by many authors (Steuber 1999; Steuber et al. 2005; Huck et al. 2013; Huck and Heimhofer 2015; Frijia et al. 2015). Well-preserved rudist specimens were collected, and the analyses were limited to the compact-shelled specimens. In order to evaluate the preservation of the original shell structures, petrographic screening of the samples for diagenetic modification was also made using a petrographic microscope. Moreover, the rudist shells with fractures, veins, and any diagenetic features were avoided. There are two possibilities for a mismatch between

the isotope data derived from the bulk samples and from the rudist shells (Fig. 6). The first possibility could be a function of diagenetic overprint, and the second may be due to climatic and paleoenvironmental changes (Fig. 6). To test for the effects of diagenetic overprint, $\delta^{13}C$ values were plotted against $\delta^{18}O$ values for Gabal Yelleg and Maaza sections. No significant correlation is observed for the data derived from the Cenomanian (R^2 = 0.12, N = 15) and the Turonian rudists (R^2 = 0.057, N = 12) at Gabal Yelleg (Fig. 6a). The $\delta^{18}O$ values of the rudist shell samples are lower than the Cretaceous marine $\delta^{18}O$ values (Norris et al. 2002; Immenhauser et al. 2005; Prokoph et al. 2008; see Fig. 6a), whereas the $\delta^{13}C$ values are similar to the marine signatures. Moreover, the present $\delta^{13}C$ values of the Cenomanian-Turonian rudists at Gabal Yelleg are similar to the $\delta^{13}C$ values of the rudists in the Campanian of Turkey (Immenhauser et al. 2005) and the Cenomanian of Egypt (El-Shazly et al. 2011), while the $\delta^{18}O$ values are lower than the latter sites (Fig. 6a). Furthermore, the $\delta^{13}C$ and $\delta^{18}O$ values measured from the rudist shells and from the bulk carbonate samples display trivial variation in $\delta^{13}C$ values (Fig. 6b, c). Although there is a moderate correlation between $\delta^{18}O$ and $\delta^{13}C$ values (R^2 = 0.46) at Gabal Maaza (Fig. 6d), the linear covariation is not considered a reliable indicator of diagenetic overprinting (Marshall 1992). Some of the $\delta^{13}C$ and $\delta^{18}O$ values at the Cenomanian of Gabal Maaza are low when compared to those from low-latitude, shallow-marine carbonates (Prokoph et al. 2008). The $\delta^{13}C$ composite curve were subdivided into 12 characteristic segments in the northern Sinai sections. The Cenomanian and Turonian carbon-isotope segments (C23–C34) were described in stratigraphic order at the Halal and Wata Formations of the exposed sections at Gabal Yelleg

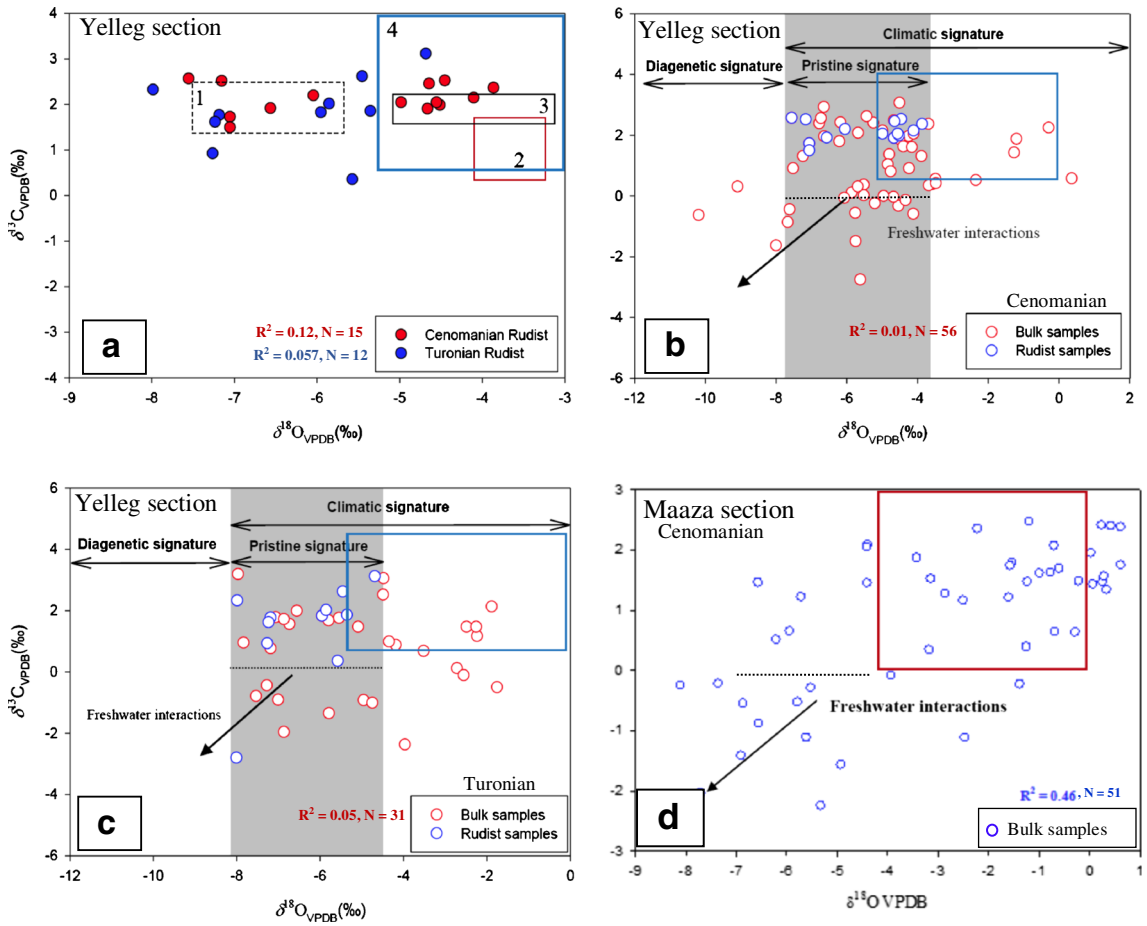

Fig. 6 Cross plots of $\delta^{13}C$ versus $\delta^{18}O$ data showing isotopic covariance **a** detected in the Cenomanian-Turonian rudists at Yelleg section; there is no correlation. Note the comparison of the present data with those of Cenomanian rudists from Egypt (*rectangle 1*; El-shazly et al. 2011), planktonic foraminifers from the Cenomanian tropical area (*rectangle 2*; Norris et al. 2002), Campanian rudists from Turkey (*rectangle 3*; Immenhauser et al. 2005), and shallow-marine biotic calcite from Cenomanian-Maastrichtian at low latitude (*rectangle 4*; Prokoph et al. 2008). **b** Data for the carbonate bulk and rudist samples from the Cenomanian at Yelleg section; there is a low correlation. Note that the values for bulk samples are affected by diagenesis and freshwater interactions, the comparison with the marine biotic calcite (*blue rectangle*; Prokoph et al. 2008) shows a decrease in the values of $\delta^{13}C$ and $\delta^{18}O$, and *below the dashed line* are freshwater interactions. **c** Data derived from the Turonian carbonate bulk and rudist samples at Yelleg section; there is a low correlation, the *blue rectangle* for marine biotic calcite from Prokoph et al. (2008). **d** Data for the carbonate bulk samples from the Cenomanian at Maaza section; there is a moderate correlation, *red rectangle* for marine biotic calcite from Prokoph et al. (2008)

(10–530 m) and Gabal Maaza (10–230 m). Here, we refer to the $\delta^{18}O$ values at sequence boundaries and flooding surfaces; however, the interpretation of the variable $\delta^{18}O$ values is beyond the scope of this study. The $\delta^{13}C$ and $\delta^{18}O$ isotope results are presented in Tables 1, 2, 3, and 4 at ESM_1.pdf. The carbon-isotope segments are described as follow (see Figs. 6, 7, 8, and 13 in ESM_2.pdf):

C23 (Lower Cenomanian), this carbon-isotope segment extends from 10 to 82 m at Gabal Yelleg and from 8 to 48 m at Gabal Maaza. The lowermost part of this segment displays a decrease in $\delta^{13}C$ values from 1.36 to −0.45‰, which continues up to 31 m at the Yelleg section. This is followed by a fluctuation in $\delta^{13}C$ between −1.64 and 2.56‰ values at the same site. A decrease in $\delta^{18}O$ values (−4.79 to −9.08‰) is seen from 10 to 40 m at Gabal Yelleg; this is followed by a fluctuation in the values between −7.66 and −5.24‰. At Gabal Maaza, segment C23 begins with a short decrease in $\delta^{13}C$ (1.79 to −0.55‰) and $\delta^{18}O$ values (−1.53 to −6.86‰) followed by a stepwise increase in $\delta^{13}C$ (−0.55 to 2.35‰) and $\delta^{18}O$ (−6.86 to −2.22‰) toward the top of this segment.

C24 (Lower Cenomanian), the $\delta^{13}C$ values fall from 2.56 to −2.76‰ (82–101 m) in the lower half of this segment, then rise to 0.51‰. This is followed by a shift to −0.57‰ to the top of the segment at 123 m above the base of Gabal Yelleg section. The range of $\delta^{18}O$ values fluctuates between −7.55 and −2.34‰ at the same location. At Gabal Maaza, the $\delta^{13}C$ values show a decrease upward to −1.12‰ in the lower part of the segment, followed by increase up to 1.87‰ at the top of this segment. Moreover, the $\delta^{18}O$ values do not show specific trends but fluctuate between −5.52 and −2.22‰.

C25 (Middle Cenomanian), the lower part (123–178 m) of this segment exhibits an upward increase in $\delta^{13}C$ (−0.57 to 2.34‰) and $\delta^{18}O$ (−5.75 to −3.68‰) values, especially at Gabal Yelleg. However, the upper part (178–195 m) of this segment shows a fluctuation in $\delta^{13}C$ values between −1.50 and 3.06‰, reaching a maximum value at the top of the segment. At the same locality, the $\delta^{18}O$ values of the upper part of this segment fluctuate around −10.18 and 0.37‰. At Gabal Maaza, the lower half (62–78 m) of this segment displays $\delta^{13}C$ values between −0.09 and 1.95‰, while $\delta^{18}O$ values range from 0.03 to −8.10‰. The $\delta^{13}C$ (1.47 to 2.40‰) and $\delta^{18}O$ (0.26 to 0.62‰) values increase in the second half (78–92 m) of this segment at Gabal Maaza.

C26 (Middle Cenomanian), the lower part (195–245 m) of this segment shows an upward decrease in $\delta^{13}C$ values from 3.06 to 0.01‰, then shows an increase to 1.03‰, and followed by a gradual decrease to 0.10‰ from 224 to 245 m at Gabal Yelleg. The $\delta^{13}C$ values at the upper part of this segment (245–272 m) exhibit a gradual increase from 0.10 to 2.92‰ at Gabal Yelleg. The $\delta^{18}O$ values of this segment at Gabal Yelleg show an overall decrease upward from −4.15 to −6.64‰. At Gabal Maaza, segment C26 begins with a decreasing trend in $\delta^{13}C$ (2.40 to −1.42‰) over 92–102 m, then increases to positive values between 0.64 and 1.74‰ at 102–135 m. At the same site, the $\delta^{18}O$ values are marked with two negative peaks of −6.90 and −6.56‰ at 103 and 135 m above the base, respectively.

C27 (Middle Cenomanian), the lowermost part of this segment (272–285 m) is characterized by a decrease in $\delta^{13}C$ values from 2.92 to −0.34‰, followed by increasing values from −0.34 to 2.38‰ at the upper part (285–299 m) of Gabal Yelleg. Moreover, $\delta^{13}C$ values of C27 at the Maaza section exhibit a decreasing trend from 1.74 to −2.25‰ (at 135–144 m) followed by a positive shift to 1.34‰ at 150 m above the base. The $\delta^{18}O$ values in the first 7 m at the base of this segment decrease from −0.28 to −4.53‰ and −1.57 to −5.32‰ at Gabal Yelleg and Maaza, respectively. This is followed by an increase in $\delta^{18}O$ values to −1.26 and 0.34‰ at the top of this segment of Gabal Yelleg and Maaza, respectively.

C28 (Upper Cenomanian), at Gabal Yelleg, this segment is characterized by a gradual increase in $\delta^{13}C$ values (from −0.04 to 2.55‰) from the base to the top of this segment (302–338 m). The $\delta^{18}O$ values fluctuate between −6.77 and −3.48‰ at the same site. In Gabal Maaza, $\delta^{13}C$ values of the lower part of this segment increase from 1.34 to 2.58‰ (150–164 m), then decrease to 1.34‰ at 169 m. This is followed by an increase in $\delta^{13}C$ values to 2.68‰ at the top of the segment (169–180 m). The $\delta^{18}O$ values fluctuate between −0.77 and 1.02‰ in this segment at Gabal Maaza.

C29 (Upper Cenomanian), at Gabal Maaza, $\delta^{13}C$ values decrease (2.68 to −2.04‰) from the base to the top of this segment at 180–218 m. At the same site, the $\delta^{18}O$ values decrease to −4.41‰ at the base of this segment, then increase to −1.25‰ at 210 m in the middle section. Over the next 8 m, the $\delta^{18}O$ values decrease to −7.70‰ at the top of the segment. At Gabal Yelleg, the $\delta^{13}C$ values exhibit a decrease from 2.55 to −0.01‰ at 338–358 m and then increase to 2.41‰ at 389 m. The coeval $\delta^{18}O$ is marked by fluctuating values between −6.72 and −1.19‰ at the same site.

C30 (Upper Cenomanian-Lower Turonian), C30 comprises the topmost part of Gabal Maaza (218–230 m). The lower part of this segment shows an increase in $\delta^{13}C$ from −2.04 to 1.69‰ followed by a decrease to −0.22‰. This decrease is subsequently followed by an increase in $\delta^{13}C$ values to 1.45‰. The $\delta^{18}O$ values in this segment at Gabal Maaza range from −7.70 to −0.60‰. The lowest portion of this segment at Gabal Yelleg has the most enriched $\delta^{13}C$ values (1.95 to 2.61‰), which decrease up to −0.25 and −0.07‰ values at 419–424 m, then increase toward the top to 1.46‰ at 428 m above the base. During this interval, $\delta^{18}O$ values range from −6.63 to −2.48‰ at Gabal Yelleg. This segment is coeval to the OAE2 interval and thus corresponds to the highest sea level during the Late Cenomanian-Early Turonian time.

C31 (Lower Turonian), in this carbon-isotope segment (428–449 m) of Gabal Yelleg, $\delta^{13}C$ values decrease from 1.46 to 0.11‰ (at 428–433 m), then rise to 1.55‰ (at 436 m). This is followed by a gradual decrease in $\delta^{13}C$ values from 1.55 to −0.92‰ (at 436–449 m). The $\delta^{18}O$ shows fluctuating values between −7.27 and −2.48‰.

C32 (Middle Turonian), this segment (449–463 m) exhibits an increase upward in the $\delta^{13}C$ values from 0.67 to 3.18‰ with a negative peak (−2.38‰) at 460 m above the base of Gabal Yelleg section. The $\delta^{18}O$ average is between −7.96 and −3.51‰.

C33 (Middle-Upper Turonian), this carbon-isotope segment occurs at 463–499 m above the base of the Yelleg section. The $\delta^{13}C$ values decrease from 3.18 to 0.93‰ at 463–470 m, followed by an increase to 1.98‰ at 475 m. This is followed by distinct negative $\delta^{13}C$ values (−1.97 to −0.80‰) from 470 to 499 m. This segment is characterized by higher negative values of $\delta^{18}O$ (from −4.74 to −7.96‰).

C34 (Upper Turonian), this segment (499–530 m at Gabal Yelleg) starts with an increasing trend of $\delta^{13}C$ (from −1.02 to 1.82‰) at 499–504 m followed by fluctuating values (between −0.51 and 2.12‰). Segment C34 ends with a shift to low values of $\delta^{13}C$ (from 2.12 to −0.12‰) at 518–530 m. The $\delta^{18}O$ values at the lowermost part of this segment are more negative than the values at the upper part.

Regional correlation and discussion

The variation between $\delta^{18}O$ and $\delta^{13}C$ values derived from the rudist shells and from the bulk carbonate samples (Fig. 6b, c) is attributed to the composition of the bulk samples that consists of an interplay of biological, sedimentological, and physicochemical processes (Wendler 2013). The change in $\delta^{13}C$ values may be explained as a result of varying amounts of aragonite in the sediments (Swart and Eberli 2005), physiology of the organisms (Schöne 2008; Huck and Heimhofer 2015), the seawater pH (Zeebe 2001), the global carbon cycles, and/or the dissolved inorganic carbon (Swart 2015). Because the rudists are carbonate-secreting organisms (Skelton and Gili 2011), the calcification rates and mechanisms may explain the variation in isotope values (Immenhauser et al. 2005; Findlay et al. 2011; Swart 2015). Furthermore, the change in the trophic conditions is also likely reflected by a variation in the carbon isotopes (Föllmi and Godet 2013).

In this study, the correlation of $\delta^{13}C$ values from bulk samples and pristine rudist shells indicated that the effect of diagenesis on most of the carbon-isotope segments is not significant throughout the majority of the studied sections. Even when there is an observed variation in the isotopic signatures due to diagenesis, the process affects the oxygen-isotopic signature more than the carbon-isotope values of the marine sediments (Weissert et al. 2008). Some of the isotopic trends could be the result of local environmental conditions rather than open ocean water (Colombie et al. 2011; Frijia et al. 2015). Thus, we concluded that the comparison of our isotope data recovered from the studied sections with those from the Late Cretaceous $\delta^{13}C$ reference curves (Wilmsen 2000, 2007; Jarvis et al. 2006; Voigt et al. 2007; Gambacorta et al. 2015) would be best achieved by including the biostratigraphic data.

The presence of low $\delta^{18}O$ and $\delta^{13}C$ values at the subaerial exposures and sequence boundaries supports the freshwater interactions and diagenetic overprint (Immenhauser et al. 2003; Armstrong-Altrin et al. 2009; Cochran et al. 2010; Elrick and Scott 2010). The negative shifts in $\delta^{18}O$ and $\delta^{13}C$ values associated with the subaerial exposure could have been the result of alteration by isotopically light meteoric waters. Furthermore, the local increase in $\delta^{18}O$ values is likely because of a high rate of evaporation, especially in the Cenomanian interval, which was possibly the warmest episode in the Cretaceous period (Norris et al. 2002).

Chemostratigraphic correlation may be achieved by ammonites, rudists, and other macrofossil biostratigraphic data in Sinai (Abdel-Gawad et al. 2004; El-Qot 2006; Saber et al. 2009; Ayoub-Hannaa and Fürsich 2012; see Table 5 at ESM_1.pdf). The documented biostratigraphic data combined with the carbon-isotope segments were utilized to enhance the chronostratigraphic calibration in the studied sections.

There are many high-resolution $\delta^{13}C$ curves for the Cenomanian-Turonian interval in Tethys. A comparison of the Cenomanian-Turonian carbon-isotope segments of the studied sections with the Tethyan $\delta^{13}C$ profiles of Wilmsen (2000 and 2007), Jarvis et al. (2006), Voigt et al. (2007), Vahrenkamp (2013), and Gambacorta et al. (2015) is based on the presence of specific isotopic values and trends, as well as the biostratigraphic data.

The Lower Cenomanian events (LCE I–III) of Jarvis et al. (2006) are compared with the carbon-isotope segment C23 that shows three well-defined positive $\delta^{13}C$ excursions with values up to 2.07, 2.40, and 2.56‰ at Gabal Yelleg (Fig. 13 at ESM_2.pdf). The negative $\delta^{13}C$ values in this segment C23 may be attributed to an increase in the organic carbon content. At Gabal Maaza, $\delta^{13}C$ values for C23 jump from −0.53 to 2.35‰; however, no peaks are observed. This $\delta^{13}C$ excursion occurred in the deeper part of the basin during the sea level rise. The fluctuations in $\delta^{13}C$ and $\delta^{18}O$ at Gabal Yelleg may have resulted from an increase in the siliciclastic input from the adjacent continent during the transgression. The Early Cenomanian age of this carbon-isotope segment is based on the occurrence of macrofossils (Abdel-Gawad et al. 2004; Table 5 at ESM_1.pdf). Moreover, the stratigraphic position of segment C23 is confirmed above the Albian-Cenomanian boundary that is defined by the occurrence of *O.* (*C*) *conica* (Saber et al. 2009).

Carbon-isotope segment C24 begins with bioturbated marl showing a decrease in $\delta^{13}C$ and $\delta^{18}O$ values followed by a positive excursion. The bioturbation was used as evidence to determine the onset of oxygen-depleted, shallow-marine environment (Kennedy and Wagner 2011). Furthermore, the bioturbation likely influenced the accumulation of organic carbon in the sediments deposited across the oxygen minimum zone (Canuel et al. 2007).

The clearly positive $\delta^{13}C$ trend at the base of C25 at Gabal Yelleg coincides with sea level rise. This increase in $\delta^{13}C$ values is attributed to an increase in the productivity and preservation of organic matter (Katz et al. 2007; Vahrenkamp 2010). Furthermore, the elevated $\delta^{18}O$ values in C25 at Gabal Maaza reflect the temperature of the marine porewaters during the period of maximum flooding (Christ et al. 2015). Within the uppermost part of segment C25, the $\delta^{13}C$ values show a decreasing trend with slight fluctuations between the negative and positive values especially at Gabal Yelleg. These fluctuations in the $\delta^{13}C$ values are indicative of submarine lithification at the maximum flooding surface (Christ et al. 2015). The absence of viable biostratigraphic data at this level makes the position of the Lower-Middle Cenomanian boundary in the studied sections somewhat uncertain. However, the position of this boundary in the Cenomanian succession in Oman is placed at a positive carbon-isotope excursion (Wohlwend et al. 2016). The pronounced positive $\delta^{13}C$ excursion at the lowermost part of C25 may encourage us to place the Lower-Middle Cenomanian boundary at the base of C25, especially at the Gabal Yelleg section. Nevertheless, this result remains equivocal. This isotope event is defined as mid-Cenomanian event I (MCE I) (Jarvis et al. 2006; Wilmsen 2000 and 2007; Gambacorta et al. 2015; Wohlwend et al. 2016). The pre-MCE I event is characterized by negative carbon excursions that are observed in carbon-isotope segment C24 in the studied sections (Fig. 13 at ESM_2.pdf). The rudist sublevel GY III (*B. africana* and *B. zumoffeni* association) is developed in the medium-scale highstand system tract 2 and at carbon-isotope segment C25.

The values of $\delta^{13}C$ decrease at the base of segment C26 at Yelleg and Maaza sections. The presence of both negative $\delta^{13}C$ and $\delta^{18}O$ values at Gabal Maaza supports the diagenesis and the interaction of freshwaters. However, this segment (C26) displays elevated $\delta^{13}C$ values that precede the carbon-isotope segment C27. A similar trend has been introduced between P/B break and MCE II events by Jarvis et al. (2006). The $\delta^{13}C$ variations observed in segment C26 of Gabal Maaza are lower than that of the shallow inner ramp facies of Gabal Yelleg. These variations in the isotopic records are attributed to the deposition of the Maaza section at the distal part of the basin, whereas the Yelleg section was deposited in the proximal part.

The negative $\delta^{13}C$ and $\delta^{18}O$ shift in segment C27 is interpreted as the result of meteoric water alteration during the subaerial exposure at SB2. The dedolomitization and the subaerial exposure features at SB2 support the decrease in $\delta^{13}C$ and $\delta^{18}O$ within this interval in both the Gabal Yelleg and Maaza sections (Rameil 2008). The Middle-Upper Cenomanian boundary is placed based on the occurrence of *N. vibrayeanus* (Abdel-Gawad et al. 2004). An increase in $\delta^{13}C$ values from −2.25 to 0.63‰ at Gabal Maaza and from −0.15 to 1.42‰ at Gabal Yelleg allowed the placement of the boundary below *N. vibrayeanus* and at the top of carbon-isotope segment C27 (Fig. 13 at ESM_2.pdf). In addition, this increase in $\delta^{13}C$ is correlated with the Jukes-Browne event (Jarvis et al. 2006) that marked the Middle-Upper Cenomanian boundary in Oman (Wohlwend et al. 2016).

The positive trend of $\delta^{13}C$ at C28 marks the lower Upper Cenomanian in the carbon curve of Jarvis et al. (2006) in Europe. This positive trend is related to sea level rise during the transgression phase of the third-order sequence 2. This segment is recorded directly above *N. vibrayeanus* zone at Gabal Yelleg. A gradual decrease in $\delta^{13}C$ values at C29 can be explained as result of changes in the rate of sedimentation during the highstand system tract (Weissert et al. 1998). However, the $\delta^{13}C$ and $\delta^{18}O$ values across the subaerial exposure SB3 suggest meteoric diagenetic alteration in the carbonate deposited below the sequence boundary, particularly at Gabal Maaza.

The Cenomanian-Turonian boundary interval is marked by a positive carbon excursion that indicates the OAE2 (Arthur et al. 1988; Leckie et al. 2002; Tsikos et al. 2004; Jarvis et al. 2006; Sageman et al. 2006; Gertsch et al. 2010; Wendler et al. 2010; El-Sabbagh et al. 2011; Nagm et al. 2014; Gambacorta et al. 2015). However, at Gabal Yelleg, the C-T boundary is placed at the onset of falling $\delta^{13}C$ values from 2.61 to −0.25‰ in the upper part of OAE2 with carbon-isotope segment C30 (Fig. 8 at ESM_2.pdf). The OAE2 is confirmed to the lattermost part of the Cenomanian, similar to many curves obtained around the world. However, the amplitude of the $\delta^{13}C$ values at the Gabal Yelleg section is lower than the other reported locations, because Yelleg section was deposited in shallow water and near the coastline, which was likely influenced by freshwater influx.

Five carbon-isotope trends have been recognized from the Turonian Wata Formation at Gabal Yelleg (Fig. 8 at ESM_2.pdf). The first trend at C30 exhibits values depleted in ^{13}C at the base and enriched toward the top. The date of this segment is confirmed by the occurrence of the Early Turonian ammonites *C. segne* and *T. rollandi.* The positive excursion corresponds to the Early Turonian Holywell event (Jarvis et al. 2006) and Tu1 event (Voigt et al. 2007). The second carbon-isotope trend (C31) shows a gradual decrease in the $\delta^{13}C$ values toward the sequence boundary 4. Higher up, the $\delta^{13}C$ values begin to increase gradually up to the top of segment C32. The inflection that occurs at the contact between carbon-isotope segments C31 and C32 from falling to rising $\delta^{13}C$

values correlates with the Lulworth event of Jarvis et al. (2006) in the English Chalk and the Tu5 events in Germany (Voigt et al. 2007). Moreover, this negative carbon-isotope shift was placed at the *M. nodosoides*/*C. woollgari* zone boundary that supports the position of this event at Lower-Middle Turonian boundary (Sageman et al. 2006; Wendler et al. 2010). The positive $\delta^{13}C$ excursion at the top of C32 correlates with the Round Down event of Jarvis et al. (2006) in English Chalk and isotope event Tu8 in Germany at the Middle Turonian (Voigt et al. 2007). The first appearance of *P. ponsianus* and *D. lombricalis* at the top of C32 segment supports the Middle Turonian age for rudist sublevel VI within the highstand system tracts of the depositional sequence 4 at Gabal Yelleg (Figs. 8 and 15 at ESM_2.pdf).

The fourth carbon-isotope trend is generally marked by the change to the lower $\delta^{13}C$ values in carbon-isotope segment C33 during the Turonian interval. This segment contains the lowest $\delta^{13}C$ values in the Turonian succession. Herein, we attributed a decrease in $\delta^{13}C$ values to marine regression and the deposition of the lowstand system tract facies. These Middle Turonian deposits have been termed the Buttum Formation by Issawi et al. (1999). This rock unit is used to describe the very shallow lagoon and tidal flat claystone and gypsum deposits, which formed during a regressive phase of sea level and the arid climatic conditions in west and east central Sinai (Abdel-Gawad 1999; Abdel-Gawad et al. 2004; Ayoub-Hannaa and Fürsich 2012). The positive carbon excursion peak within segment C33 at Gabal Yelleg (Fig. 8 at ESM_2.pdf) is compared with the Low-*woollgari* event of Jarvis et al. (2006) and Tu11 event of Voigt et al. (2007). The inflection from the positive to negative $\delta^{13}C$ values is a result of transporting the plant materials that affected the bulk organic ^{13}C of the marine sediments during the lower sea level at the Middle Turonian. Shahin (2007) attributed the negative $\delta^{13}C$ values at the Wata Formation to reduced surface water productivity and progressive oxidation of organic matter. Therefore, the equivalent ostracodal wackestone facies in Gabal Yelleg section may reflect local carbon- and oxygen-isotopic signatures of the low sea level and warm climatic conditions. The *D. arnaudi* and *D. gaensis* association (rudist sublevel VII) that occurs during the highstand system tract of sequence 4 is considered to be of Middle Turonian age by correlation with the same association at Abu Roash area of north Western Desert (Abdel-Gawad et al. 2011).

The carbon segment C34 is the last isotopic interval in the Turonian at Gabal Yelleg (Fig. 8 at ESM_2.pdf). The base of this segment is compared with the Caburn event in Europe (Jarvis et al. 2006). This segment C34 is placed at the base of *C. requienianum*-bearing marl that confirms the early Late Turonian age (El-Qot et al. 2009; Gertsch et al. 2010). The rudist sublevel VIII with association of *R.* cf. *lewyi lewyi* and *R. sauvagesi* is recorded at the base of carbon-isotope segment C34. This comparison provides evidence for the late Middle Turonian age for this rudist sublevel.

The distribution and diversity of the rudists through the Cenomanian-Turonian succession are influenced by the change in the trophic conditions (Fig. 14 at ESM_2.pdf). All the rudist sublevels occur in the highstand of the medium-scale sequences except for rudist sublevel V that occurs in the transgressive system tracts and tolerates the mesotrophic conditions (Fig. 14 at ESM_2.pdf). The disappearance of the Upper Cenomanian rudists except for *E. liratus* from the early transgressive phase of the third-order sequence 2 coincides with the loss of *Praealveolina* foraminifera before the C-T boundary. The extinction of alveolinid foraminifera that occurs near the C-T boundary has been attributed to the change in trophic conditions to meso-eutrophic environments (Calonge et al. 2002; Parente et al. 2008). The absence of the rudists from sequence 3 at Gabal Yelleg may be related to the flooding of the platform during the Upper Cenomanian and the presence of the eutrophic conditions that disturbed the accumulation of rudists around the Cenomanian-Turonian interval (Lebedel et al. 2015). The rudists flourished again on the carbonate platform during the Middle Turonian with new species of these genus *Praeradiolites*, *Durania*, and *Radiolites*.

Finally, the negative carbon- and oxygen-isotope excursion is observed beneath the sequence boundary (Immenhauser et al. 2001). This negative excursion indicated that the Cenomanian-Turonian successions were prone to diagenesis. However, most of these carbonates still preserve the global carbon-isotope signals. In the present study, the negative shifts in $\delta^{13}C$ and $\delta^{18}O$ match the third-order sequence boundaries 2, 4, and 5 (Fig. 15 at ESM_2.pdf). Moreover, the transgressive system tracts exhibit an increase in $\delta^{13}C$ values in sequences 2 and 4. In most of the third-order sequences, the $\delta^{13}C$ show increasing values toward the maximum flooding zones (Fig. 15 at ESM_2.pdf). However, the regressive phase of the depositional sequences coincides with the lower $\delta^{13}C$ values (Immenhauser et al. 2003).

Conclusion

This study demonstrated that shallow-water deposits could preserve the carbon-isotope events that are defined in the pelagic successions. This paper documented the $\delta^{13}C$ and $\delta^{18}O$ values for the entire Cenomanian-Turonian succession in north Sinai and correlated these isotope data with those from the nearby areas. The variation in the carbon- and oxygen-isotopic signatures of the rudist shells and the bulk carbonate samples is explained as a result of paleoenvironmental conditions and

diagenetic overprint. Based on the general trend and the absolute values of $\delta^{13}C$, the present carbon-isotopic segments can be correlated with global carbon-isotope events. The $\delta^{13}C$ positive excursion at the OAE2 is associated with latest Cenomanian sea transgression. An isotopic depletion associated with the sequence boundaries indicates interaction with isotopically light meteoric water during the subaerial exposure. Therefore, the negative $\delta^{13}C$ values at these boundaries do not represent a global marine isotopic signal. On the other hand, the fluctuations of the $\delta^{13}C$ values across the maximum flooding zone may be attributed to the degree of lithification during this interval. The prominent negative $\delta^{13}C$ values at the Middle Turonian carbon-isotope segment C33 confirm the influence of sea level on the isotopic signatures.

The integration of the rudist levels, carbon-isotope segments, ammonite zonation, and sequence stratigraphy data allowed us to set the rudists in the precise position within the transgressive-regressive cycles. The data suggests the Lower Cenomanian for rudist sublevels GY I and II and Middle Cenomanian for rudist sublevel III in the highstand system tracts of the fourth-order sequences. However, the late Middle Cenomanian rudist sublevel IV occurs in the highstand system tracts of the third-order sequence 1. Above the *N. vibrayeanus*, the Upper Cenomanian rudist level V that contains the *E. liratus* is the only rudist formed in the carbonate platform during the Late Cenomanian. The absence of the rudists from the Upper Cenomanian-Lower Turonian sequence may be attributed to the drowning of the platform and the domination of the eutrophic conditions.

Acknowledgements We have greatly appreciated the helpful suggestions and comments of the Editor and reviewers. I sincerely thank Prof. Dr. Bill Harrison, Linda Harrison, and Sue Grammer (MGRRE, Western Michigan University, USA) for their never-ending enthusiasm and allowing me to use the facility. I thank Mohamed El-Shenawy from MRSI laboratory at McMaster University for his fruitful discussion. A special note of thanks goes to Stable Isotope Laboratory (SIL) at University of Miami, USA, for the carbon- and oxygen-isotope analyses. Financial support by the Egyptian Missions Sector for this work is gratefully acknowledged.

References

Abdallah AM, Abdel-Gawad GI, Mekawy MS (2001) Stratigraphy of the Cenomanian and Turonian sequence of El-Giddi Pass, northwest Sinai, Egypt. Egypt. Proc. 6th Conf. Geol Sinai Develop 211–229

Abdallah AM, Aboul Ela NM, Saber SG (1996) Lithostratigraphy, microfacies and depositional environments of the Cretaceous rocks at Gabal Halal area, northern Sinai, Egypt. 3rd Int Conf Geol Arab World, Cairo University 381–406

Abdel-Gawad, GI (1999) Biostratigraphy and facies of the Turonian in west central Sinai, Egypt. Ann Geol Surv Egypt, XXII, 99–114. Cairo

Abdel-Gawad GI, Zalat A (1992) Some Upper Cretaceous macroinvertebrates from Gebel El-Hamra and Gebel Um-Heriba, Mitla pass, western-central Sinai, Egypt. 1st Int Conf Geol Arab World, Gaw 1, Cairo University 321–332

Abdel-Gawad GI, El Sheikh HA, Abdelhamid MA, El Beshtawy MK, Abed MM, Fürsich FT, El-Qot GM (2004) Stratigraphic studies on some the Upper Cretaceous successions in Sinai, Egypt. Egypt J Paleont 4:263–303

Abdel-Gawad GI, Saber SG, El Shazly SH, Salama YF (2011) Turonian rudist facies from Abu Roash area, north Western Desert, Egypt. J Afr Earth Sci 59:359–372

Al-Ghamdi N, Read JF (2010) Facies-based sequence stratigraphic framework of the Lower Cretaceous rudist platform, Shu'aiba Formation, Shaybah field, Saudi Arabia. In F.S.P van Buchem, M.I. Al-Husseini, F. Maurer and H.J. Droste (eds.). Aptian stratigraphy and petroleum habitat of the eastern Arabian plate. GeoArabia Spec Publ 4:367–410

Aly MF, Saber SG, Abdel-Gawad GI, Salama YF (2005) Cenomanian–Turonian rudist buildups of northern Sinai, Egypt. Egypt J Paleont 5: 253–286

Armstrong-Altrin JS, Lee YI, Verma SP, Worden RH (2009) Carbon, oxygen, and strontium isotope geochemistry of carbonate rocks of the upper Miocene Kudankulam Formation, southern India: implications for paleoenvironment and diagenesis. Chemie der Erde - Geochemistry 69(1):45–60

Arthur MA, Dean WE, Pratt LM (1988) Geochemical and climatic effects of increased marine organic carbon burial at the Cenomanian/Turonian boundary. Nature 335:714–717

Ayoub-Hannaa WS, Fürsich FT (2012) Cenomanian-Turonian ammonites from eastern Sinai, Egypt, and their biostratigraphic significance. Beringeria 42:57–92

Bachmann M, Bassiouni MAA, Kuss J (2003) Timing of mid-Cretaceous carbonate platform depositional cycles, northern Sinai, Egypt. Palaeogeogr Palaeoclimatol Palaeoecol 200:131–162

Bachmann M, Kuss J, Lehmann J (2010) Controls and evolution of facies patterns in the upper Barremian-Albian Levant platform in North Sinai and Israel. In C. Homberg and M. Bachmann (eds.), evolution of the Levant margin and western Arabia platform since the Mesozoic. Geol Soc Lond Spec Publ 341:99–131

Batenburg SJ, De Vleeschouwer D, Sprovieri M, Hilgen FJ, Gale AS, Singer BS, Koeberl C, Coccioni R, Claeys P, Montanari A (2016) Orbital control on the timing of oceanic anoxia in the Late Cretaceous. Clim Past Discuss. doi:10.5194/cp-2015-182

Bauer J, Marzouk A, Steuber T, Kuss J (2001) Lithostratigraphy and biostratigraphy of the Cenomanian-Santonian strata of Sinai, Egypt. Cretac Res 22:497–526

Bauer J, Steuber T, Kuss J, Heimhofer U (2004) Distribution of shallow-water benthics (rudists, calcareous algae, benthic foraminifers) in the Cenomanian-Turonian carbonate platform sequences of Sinai, Egypt. Courier Forschungsinstitut Senckenberg 247:207–231

Bover-Arnal T, Salasb R, Moreno-Bedmarb JA, Bitzera K (2009) Sequence stratigraphy and architecture of a late early–middle Aptian carbonate platform succession from the western Maestrat Basin (Iberian chain, Spain). Sediment Geol 219:280–301

Calonge A, Caus E, Bernaus JM, Aguilar M (2002) Praealveolina (foraminifera) species: a tool to date Cenomanian platform sediments. Micropaleont 48:53–66

Canuel EA, Spivak AC, Waterson EJ, Duffy JE (2007) Biodiversity and food web structure influence short-term accumulation of sediment organic matter in an experimental seagrass system. Limnol Oceanogr 52(2):590–602

Christ N, Immenhauser A, Wood RA, Darwich K, Niedermayr A (2015) Petrography and environmental controls on the formation of Phanerozoic marine carbonate hardgrounds. Earth Sci Rev 151: 176–226

Cochran JK, Kallenberg K, Landman NH, Harries PJ, Weinreb D, Turekian KK, Beck AJ, Cobban W (2010) Effect of diagenesis on the Sr, O nd C isotope composition of Late Cretaceous molluscs from the western interior seaway of North America. Americ J Sci 310:69–88

Colombie C, Lecuyer C, Strasser A (2011) Carbon- and oxygen-isotope records of palaeoenvironmental and carbonate production changes in shallow-marine carbonates (Kimmeridgian, Swiss Jura). Geol Magaz 148:133–153

De Castro P, Sirna G (1996) The *Durania arnaudi* biostrome of El-Hassana, Abu Roash area, Egypt. Geol Romana 32:69–91

Dickson AJ, Saker-Clark M, Jenkyns HC et al (2016) A southern hemisphere record of global trace-metal drawdown and orbital modulation of organic-matter burial across the Cenomanian–Turonian boundary (Ocean Drilling Program site 1138, Kerguelen Plateau). Sedimentol doi. doi:10.1111/sed.12303

Droste HJ (2010) High-resolution seismic stratigraphy of the Shu'aiba and Natih Formations in the Sultanate of Oman: implications for Cretaceous epeiric carbonate platform systems. In: van Buchem, F.S.P., Gerdes, K.D. & Esteban, M. (eds) Mesozoic and Cenozoic carbonate systems of the Mediterranean and the Middle East—stratigraphic and diagenetic reference models. Geol Soc Lond Spec Publ 329:145–162

Elderbak K, Leckie RM, Tibert NE (2014) The Cenomanian–Turonian boundary event (oceanic anoxic event 2) as indicated by foraminiferal assemblages from the eastern margin of the Cretaceous western Interior Sea. Palaeogeogr Palaeoclimatol Palaeoecol 413:29–48

El-Hedeny MM (2007) New taxonomic and biostratigraphic data on the Upper Cenomanian-Turonian Radiolitidae (bivalvia: Hippuritoidea) of Abu Roash, Western Desert, Egypt. Neues Jahrbuch fur Geologie und Palaontologie Abhandlungen 244(1):79–98

El-Hedeny MM, El-Sabbagh AM (2005) *Eoradiolites liratus* (bivalvia, Radiolitidae,) from the Upper Cenomanian at Saint Paul, Eastern Desert (Egypt). Cretac Res 26:551–566

EL-Qot GM (2006) Late Cretaceous macrofossils from Sinai, Egypt. Beringeria 36:3–163

EL-Qot GM, Fürsich FT, Abdel-Gawad GI, Ayoub-Hannaa WS (2009) Taxonomy and palaeoecology of Cenomanian-Turonian (Upper Cretaceous) echinoids from eastern Sinai, Egypt. Beringeria 40: 55–98

Elrick M, Scott LA (2010) Carbon and oxygen isotope evidence for high-frequency (104–105 yr) and my-scale glacioeustasy in middle Pennsylvanian cyclic carbonates (Gray Mesa Formation), central New Mexico. Palaeogeogr Palaeoclimatol Palaeoecol 285:307–320

El-Sabbagh A, Tantawy AA, Keller G, Khozyem H, Spangenberg J, Adatte T, Gertsch B (2011) Stratigraphy of the Cenomanian–Turonian oceanic anoxic event OAE2 in shallow shelf sequences of NE Egypt. Cretac Res 32:705–722

El-Shazly S, Košták M, Abdel-Gawad G, Kloučková B, Saber S, Salama YF, Mazuch M, Žák K (2011) Carbon and oxygen isotopes of selected Cenomanian and Turonian rudists from Egypt and Czech Republic, and a note on changes in rudist diversity. Bull Geosci 86(2):209–226

El-Shinnawi MA, Sultan I (1973) Lithostratigraphy of some subsurface Upper Cretaceous sections in the Gulf of Suez area. Egypt, Acta Geol Hungaria 17:469–493

Embry JC, Vennin E, Van Buchem FSP, Schroeder R, Pierre C, Aurell M (2010) Sequence stratigraphy and carbon isotope stratigraphy of an Aptian mixed carbonate-siliciclastic platform to basin transition (Galve sub-basin, NE Spain). Geol Soc Lond Spec Publ 329:113–143

Findlay HS, Wood HL, Kendall MA, Spicer JI, Twitchett RJ et al (2011) Comparing the impact of high CO_2 on calcium carbonate structures in different marine organisms. Mar Biol Res 7:565–575

Föllmi KB, Godet A (2013) Palaeoceanography of Lower Cretaceous alpine platform carbonates. Sedimentol 60:131–151

Friedrich O, Erbacher J, Mutterlose J (2006) Paleoenvironmental change across the Cenomanian/Turonian boundary event [oceanic anoxic event 2] as indicated by benthic foraminifera from the Demerara rise [ODP leg 207]. Rev Micropaléont 49:121–139

Frijia G, Parente M, Di Lucia M, Mutti M (2015) Carbon and strontium isotope stratigraphy of the Upper Cretaceous (Cenomanian-Campanian) shallow-water carbonates of southern Italy: chronostratigraphic calibration of larger foraminifera biostratigraphy. Cretac Res 53:110–139

Gale AS, Bown P, Caron M, Crampton J, Crowhurst SJ, Kennedy WJ, Petrizzo MR, Wray DS (2011) The uppermost middle and upper Albian succession at the col de Palluel, Hautes Alpes, France: an integrated study (ammonites, inoceramid bivalves, planktonic foraminifera, nannofossils, geochemistry, stable oxygen and carbon isotopes, cyclostratigraphy). Cretac Res 32:59–130

Gambacorta G, Jenkyns HC, Russo F, Tsikos H, Wilson PA, Faucher G, Erba E (2015) Carbon- and oxygen-isotope records of mid-Cretaceous Tethyan pelagic sequences from the Umbria–Marche and Belluno basins (Italy). Newsl Stratigr 48(3):299–323

Gambacorta G, Bersezio R, Weissert H, Erba E (2016) Onset and demise of Cretaceous oceanic anoxic events: the coupling of surface and bottom oceanic processes in two pelagic basins of the western Tethys. Paleoceanography 31(6):732–757

Gebhardt H, Friedrich O, Schenk B, Fox L, Hart M, Wagreich M (2010) Paleoceanographic changes at the northern Tethyan margin during the CenomanianeTuronian oceanic anoxic event (OAE2). Mar Micropaleontol 77:25–45

Gertsch B, Keller G, Adatte T, Berner Z, Kassab AS, Tantawy AA, El-Sabbagh M, Stueben D (2010) Cenomanian–Turonian transition in a shallow water sequence of the Sinai, Egypt. Int J Earth Sci 99(1): 165–182

Ghanem H, Mouty M, Kuss H (2012) Biostratigraphy and carbon-isotope stratigraphy of the uppermost Aptian to Late Cenomanian strata of the south Palmyrides, Syria. Geoarabia 17(2):155–184

Ghorab MA (1961) Abnormal stratigraphic features in Ras Gharib oil field, Egypt. Proc 3rd. Arab Petrol Cong 2:1–10

Hamama H (2010) Morphology and wall structure of some Turonian rudists (bivalvia, Hippuritoida) of Gabal Yelleg, northern Sinai, Egypt. J Amer Sci 6(12):1682–1701

Haq BU, Hardenbol J, Vail PR (1988) Mesozoic and Cenozoic chronostratigraphy and eustatic cycles. In: Wilgus CK, Hastings BS, Kendall GStC, Possamentier HW, Ross CA, Van Wagoner JC (Eds) Sea level Changes: An Integrated Approach Society of Economic Palaeontologists and Mineralogists Spec Pub 42: 71–108

Hassan MM, Abdel Hafez NA, Dardir AA, Arian MA (1992) Geologic studies on the Cretaceous sedimentary rocks in Risan Aneiza-G. Al Amrar area, northern Sinai, Egypt. 1st Int Conf Geol. Arab World Gaw 1:353–364

Huck S, Heimhofer U (2015) Improving shallow-water carbonate chemostratigraphy by means of rudist bivalve sclerochemistry. Geochem Geophy Geosyst 16(9):3111–3128

Huck S, Heimhofer U, Immenhauser A, Weissert H (2013) Carbon-isotope stratigraphy of Early Cretaceous (Urgonian) shoal-water deposits: Diachronous changes in carbonate-platform production in the north-western Tethys. Sediment Geol 290:157–174

Immenhauser A, Della Porta G, Kenter JAM (2003) An alternative model for positive shifts in shallow-marine carbonate $\delta^{13}C$ and $\delta^{18}O$. Sedimentol 50:953–959

Immenhauser A, van der Kooij B, van Vliet A, Schlager W, Scott RW (2001) An ocean facing Aptian-Albian carbonate margin, Oman. Sedimentol 48:1187–1207

Immenhauser A, Nagler TF, Steuber T, Hippler D (2005) A critical assessment of mollusk $^{18}O/^{16}O$, Mg/Ca, and $^{44}Ca/^{40}Ca$ ratios as proxies for Cretaceous seawater temperature seasonality. Palaeogeogr Palaeoclim Palaeoecol 215:221–237

Issawi B, El-Hinnawi M, Francis M, Mazhar A (1999) The Phanerozoic geology of Egypt: a geodynamic approach. Egy Geol Surv Spec Publi 76:462

Jarvis I, Gale AS, Jenkyns HC, Pearce MA (2006) Secular variation in Late Cretaceous carbon isotopes: a new $\delta^{13}C$ carbonate reference curve for the Cenomanian-Campanian (99.6–70.6 Ma). Geol Mag 143:561–608

Jenkyns HC, Dickson AJ, Ruhl M, Van Den Boorn SHJM (2016) Basalt–seawater interaction, the Plenus cold event, enhanced weathering and geochemical change: deconstructing OAE2 (Cenomanian–Turonian, Late Cretaceous). Sedimentol Accepted article. doi:10.1111/sed.12305

Kassab AS, Obaidalla NA (2001) Integrated biostratigraphy and interregional correlation of the Cenomanian–Turonian deposits of Wadi Feiran, Sinai, Egypt. Cretac Res 22:1–11

Katz DA, Bouniconti MR, Montanez IP, Swart PK, Eberli GP, Smith LB (2007) Timing and local perturbations to the carbon pool in the lower Mississippian Madison limestone, Montana and Wyoming. Palaeogeogr Palaeoclim Palaeoecol 256(3–4):231–253

Kauffman EG (1995) Global change leading to biodiversity crisis in a greenhouse world: the Cenomanian-Turonian (Cretaceous). In: Effects of past global change on life. Nat Res Counc, National Academy Press, Washington, D.C., pp. 47–71

Keller G, Pardo A (2004) Age and paleoenvironment of the Cenomanian–Turonian global stratotype section and point at Pueblo, Colorado. Mar Micropaleont 51:95–128

Kennedy MJ, Wagner T (2011) Clay mineral continental amplifier for marine carbon sequestration in a greenhouse ocean. Proc Nat Acad Sci USA 108(24):9776–9781

Kora M, Genedi A (1995) Lithostratigraphy and facies development of Upper Cretaceous carbonates in east central Sinai, Egypt. Facies 32: 223–236

Kuss J, Bachmann M (1996) Cretaceous paleogeography of the Sinai Peninsula and neighbouring area. Comptes Rendus de l'Academie des Sciences, Serie IIa 322:915–933

Lebedel V, Lézin C, Andreu B, Ettachfini ELM, Grosheny D (2015) The Upper Cenomanian–Lower Turonian of the Preafrican trough (Morocco): platform configuration and palaeoenvironmental conditions. J Afr Earth Sci 106:1–16

Leckie RM, Bralower TJ, Cashman R (2002) Oceanic anoxic events and plankton evolution: biotic response to tectonic forcing during the mid-Cretaceous. Paleoceanography 17:13–29

Lüning S, Kuss J, Bachmann M, Marzouk A, Morsi A (1998) Sedimentary response to basin inversion: mid Cretaceous-Early Tertiary pre-to syndeformational deposition at the Areif el Naqa anticline (Sinai, Egypt). Facies 38:103–136

Marshall JD (1992) Climatic and oceanographic isotopic signals from the carbonate rock record and their preservation. Geol Magaz 129:143–160

Moosavizadeh SMA, Mahboubi A, Kavoosi RMMA, Schlagintweit F (2015) Sequence stratigraphy and platform to basin margin facies transition of the Lower Cretaceous Dariyan Formation (northeastern Arabian plate, Zagros fold-thrust belt, Iran). Bull Geosci 90:145–172

Nagm E, El-Qot G, Wilmsen M (2014) Stable-isotope stratigraphy of the Cenomanian–Turonian (Upper Cretaceous) boundary event (CTBE) in Wadi Qena, Eastern Desert, Egypt. J Afr Earth Sci 100:524–531

Norris RD, Bice KL, Magno EA, Wilson PA (2002) Jiggling the tropical thermostat in the Cretaceous hothouse. Geology 30:299–302

Özer S, Ahmad F (2015) Cenomanian–Turonian rudist (bivalvia) lithosomes from NW of Jordan. J Afr Earth Sci 107:119–137

Parente M, Frijia G, Di Lucia M, Jenkyns HC, Woodfine RG, Baroncini F (2008) Stepwise extinction of larger foraminifera at the Cenomanian–Turonian boundary: a shallow-water perspective on nutrient fluctuations during oceanic anoxic event 2 (Bonarelli event). Geology 36(9):715–718

Parnes A (1987) Radiation of species of the genus radiolites from the Upper Turonian at G. Er-Risha, NE Sinai, Egypt. Geol Sur Isr 135–153

Philip J, Airaud-Crumiere C (1991) The demise of the rudist bearing carbonate platform at the Cenomanian/Turonian boundary: a global control. Coral Reefs 10:115–125

Prokoph A, Shields GA, Veizer J (2008) Compilation and time-series analysis of a marine carbonate $\delta^{18}O$, $\delta^{13}C$, $^{87}Sr/^{86}Sr$ and $\delta^{34}S$ database through Earth history. Earth-Sci Rev 87:113–133

Rameil N (2008) Early diagenetic dolomitization and dedolomitization of Late Jurassic and earliest Cretaceous platform carbonates: a case study from the Jura Mountains (NW Switzerland, E France). Sedim Geol 212(1–4):70–85

Razin P, Taati F, van Buchem FSP (2010) Sequence stratigraphy of Cenomanian–Turonian carbonate platform margins (Sarvak Formation) in the high Zagros, SW Iran: an outcrop reference model for the Arabian plate. In: van Buchem, FSP, Gerdes KD, Esteban M (eds) Mesozoic and Cenozoic carbonate systems of the Mediterranean and the Middle East stratigraphic and diagenetic reference models. Geol Soc London Spec Pub 329:187–218

Reolid M, Sáónchez-Quinónez CA, Alegret L, Molina E (2015) Palaeoenvironmental turnover across the Cenomanian-Turonian transition in Oued Bahloul, Tunisia: foraminifera and geochemical proxies. Palaeogeogr Palaeoclimat Palaeoec 417:491–510

Saber SG (2002) Depositional facies and paleoenvironments of the Cenomanian–Santonian succession in Gabal Ekma, west central Sinai, Egypt. Egy J Geol 46(2):471–494

Saber SG (2012) Depositional framework and sequence stratigraphy of the Cenomanian–Turonian rocks on the western side of the Gulf of Suez, Egypt. Cretac Res 37:300–318

Saber SG, Salama YF, Scott RW, Abdel-Gawad GI, Aly MF (2009) Cenomanian-Turonian rudist assemblages and sequence stratigraphy on the north Sinai carbonate shelf, Egypt. Geoarabia 14(4):113–134

Sageman BB, Meyers SR, Arthur MA (2006) Orbital time scale and new C-isotope record for Cenomanian–Turonian boundary stratotype. Geology 34:125–128

Sari B, Özer S (2009) Upper Cretaceous rudist biostratigraphy of the Bey Dag˘ları carbonate platform, western Taurides; SW Turkey. Geobios 42:359–380

Sari B, Steuber T, Özer S (2004) First record of Upper Turonian rudists (Mollusca, Hippuritoidae) in the Bey Daglari carbonate platform, western Taurides (Turkey): taxonomy and strontium isotope stratigraphy of *Vaccinites praegiganteus* (Toucas, 1904). Cretac Res 25: 235–248

Schöne BR (2008) The curse of physiology challenges and opportunities in the interpretation of geochemical data from mollusk shells. Geo Marine Lett 28:269–285

Schroeder R, Neumann M (1985) Les grands foraminifér̀s du Crétacé moyen de la région méditerranneenne. Geobios Mem Spec 7:161

Schulze F, Lewy Z, Kuss J, Gharaibeh A (2003) Cenomanian–Turonian carbonate platform deposits in west-Central Jordan. Int J Earth Sci (Geol Rundsch) 92:641–660

Scott RW (2010) Numerical ages of selected rudist bivalvia: preliminary results. Turk J Earth Sci 19:769–790

Shahin A (2007) Oxygen and carbon isotopes and foraminiferal biostratigraphy of the Cenomanian-Turonian succession in Gabal Nezzazat, southwestern Sinai, Egypt. Revue de Paléobio, Gen 26(2):359–379

Shahin A, Kora M (1991) Biostratigraphy of some Upper Cretaceous successions in the eastern central Sinai, Egypt. Neues Jahrbuch fur Geologie und Palaontologie, Monatshefte: 671–692

Simone L, Carannate G, Ruberti D, Sirna M, Sirna G, Laviano A, Tropeano M (2003) Develoment of rudist lithosomes in the Coniacian-Lower Campanian carbonate shelves of central-southern Italy: high-energy V_s low-energy settings. Palaeogeogr Palaeoclimatol Palaeoecol 200:5–29

Skelton PW, Gili E (2011) Rudists and carbonate platforms in the Aptian: a case study on biotic interactions with ocean chemistry and climate. Sedimentol 59:81–117

Steuber T, Bachmann M (2002) Upper Aptian-Albian rudist bivalves from northern Sinai, Egypt. Palaeont 45:725–749

Steuber T (1999) Isotopic and chemical intra-shell variations in low-Mg calcite of rudist bivalves (Mollusca: Hippuritacea): disequilibrium fractionations and Late Cretaceous seasonality. Int J Earth Sci 88:551–570

Steuber T, Korbar T, Jelaska V, Gusic I (2005) Strontium isotope stratigraphy of Upper Cretaceous platform carbonates of the island of Brac (Adriatic Sea, Croatia): implications for global correlation of platform evolution and biostratigraphy. Cretac Res 26:741–756

Strohmenger CJ, Steuber T, Ghani A, Barwick DG, Al-Mazrooei SHA, Al Zaabi NO (2010) Sedimentology and chemostratigraphy of the Hawar and Shu'aiba depositional sequences, Abu Dhabi, United Arab Emirates. In: van Buchem FSP, Al-Husseini MI, Maurer F, Droste HJ (eds) Barremian–Aptian stratigraphy and hydrocarbon habitat of the eastern Arabian plate. Geoarabia Spec Pub 4(2):341–365

Swart PK, Cantrell DL, Westphal H, Handford CR, Kendall CG (2005) Origin of dolomite in the Arab-D reservoir from the Ghawar field, Saudi Arabia: evidence from petrographic and geochemical constraints. J Sediment Res 75(3):476–491

Swart PK, Eberli GP (2005) The nature of the $d^{13}C$ of Periplatform sediments: implications for stratigraphy and the global carbon cycle. Sediment Geol 175(1–4):115–129

Swart PK, Melim LA (2000) The origin of dolomites in Tertiary sediments from the margin of Great Bahama Bank. J Sediment Res 70:738–748

Swart PK (2015) The geochemistry of carbonate diagenesis: the past, present and future. Sedimentol 62(5):1233–1304

Tsikos H, Jenkyns HC, Walsworth-Bell B, Petrizzo MR, Forster A, Kolonic S, Erba E, Premoli Silva I, Baas M, Wagner T, Sinninghe Damste JS (2004) Carbon-isotope stratigraphy recorded by the Cenomanian–Turonian oceanic anoxic event: correlation and implications based on three key localities. J Geol Soc Lond 161:711–719

Turgeon SC, Creaser RA (2008) Cretaceous anoxic event 2 triggered by a massive magmatic episode. Nature 454:323–326

Vahrenkamp VC (2010) Chemostratigraphy of the Lower Cretaceous Shu'aiba Formation: a $\delta^{13}C$ reference profile for the Aptian stage from the southern neo-Tethys Ocean. In van Buchem FSP, Al-Husseini MI, Maurer F, Droste HJ (eds) Barremian–Aptian stratigraphy and hydrocarbon habitat of the eastern Arabian plate. Geoarabia Spec Pub 4(1):107–137

Vahrenkamp VC (2013) Carbon-isotope signatures of Albian to Cenomanian (Cretaceous) shelf carbonates of the Natih Formation, Sultanate of Oman. Geoarabia 18:65–82

Vail, P.R., Audemard, F., Bowman, S.A., Eisner, P.N., Perez-Cruz, C., 1991. The stratigraphic signatures of tectonics, eustasy and sedimentology—an overview. In: Einsele G, Ricken W, Seilacher A (eds) Cycles and Events in Stratigraphy. Springer–Verlag 617–659.

van Buchem FSP, Homewood PRPW, Oterdoom H, Philip J (2002) Stratigraphic organization of carbonate ramps and organic rich intrashelf basins: Natih Formation (Middle Cretaceous) of northern Oman. AAPG Bull 86(1):21–53

van Buchem FSP, Al-Husseini MI, Maurer F, Droste HJ, Yose LA (2010) Sequence stratigraphic synthesis of the Barremian–Aptian of the eastern Arabian plate and implications for the petroleum habitat. In van Buchem FSP, Al-Husseini MI, Maurer F, Droste HJ (eds) Barremian–Aptian stratigraphy and hydrocarbon habitat of the eastern Arabian plate. Geoarabia Spec Pub 4(1):9–48

van Buchem FSP, Razin P, Homewood PW et al (1996) High resolution sequence stratigraphy of the Natih Formation (Cenomanian/Turonian) in northern Oman: distribution of source rocks and reservoir facies. Geoarabia 1(1):65–91

van Buchem FSP, Simmons MD, Droste HJ, Davies RB (2011) Late Aptian to Turonian stratigraphy of the eastern Arabian plate—depositional sequences and lithostratigraphic nomenclature. Petrol Geosci 17:211–222

Van Helmond NAGM, Sluijs A, Reichart GJ, Sinninghe Damsté JS, Slomp CP, Brinkhuis H (2014) A perturbed hydrological cycle during oceanic anoxic event 2. Geology 42:123–126

Vicens EG, López G, Obrador A (1998) Facies successions, biostratigraphy and rudist faunas of Coniacian to Santonian platform deposits in the Sant Corneli anticline (southern central Pyrenees). In: masse J-P, Skelton PW (eds) Quatrième Congrès international Sur les Rudistes. Geobios, MS 22:403–427

Vincent B, van Buchem FSP, Bulot LG, Immenhauser A, Caron M, Baghbani D, Huc AY (2010) Carbon-isotope stratigraphy, biostratigraphy and organic matter distribution in the Aptian–lower Albian successions of southwest Iran (Dariyan and Kazhdumi Formations). In van Buchem FSP, Al-Husseini MI, Maurer F, Droste HJ (eds) Barremian–Aptian stratigraphy and hydrocarbon habitat of the eastern Arabian plate. Geoarabia Spec Pub 4(1):139–197

Voigt S, Aurag A, Leis F, Kaplan U (2007) Late Cenomanian to Middle Turonian high-resolution carbon isotope stratigraphy: new data from the Munsterland Cretaceous basin, Germany. Earth Planet Sci Lett 253:196–210

Weissert H, Joachimski MM, Sarnthein M (2008) Chemostratigraphy. Newsl Stratigr 42:145–179

Weissert H, Lini A, Föllmi KB, Kuhn O (1998) Correlation of Early Cretaceous carbon isotope stratigraphy and platform drowning events: a possible link? Palaeogeogr Palaeocl 137:189–203

Wendler JE, Lehmann J, Kuss J (2010) Orbital time scale, intra-platform basin correlation, carbon isotope stratigraphy, and sea level history of the Cenomanian/Turonian eastern Levant platform, Jordan. Geol Soc Lond Spec Publ 341:171–186

Wendler JE, Wendler I, Vogt C, Kuss J (2016) Link between cyclic eustatic sea-level change and continental weathering: evidence for aquifer-eustasy in the Cretaceous. Palaeogeogr Palaeocl 441:430–437

Wendler I (2013) A critical evaluation of carbon isotope stratigraphy and biostratigraphic implications for Late Cretaceous global correlation. Earth Sci Rev 126:116–146. doi:10.1016/j.earscirev.2013.08.003

Wilmsen M (2000) Late Cretaceous nautilids from northern Cantabria, Spain. Acta Geol Polon 50(1):29–43

Wilmsen M (2007) Integrated stratigraphy of the upper lower–lower middle Cenomanian of northern Germany and southern England. Acta Geol Polon 57(3):263–279

Wohlwend S, Hart M, Weissert H (2015) Ocean current intensification during the Cretaceous oceanic anoxic event 2—evidence from the northern Tethys. Terra Nov. 27:147–155

Wohlwend S, Hart M, Weissert H (2016) Chemostratigraphy of the upper Albian to mid-Turonian Natih Formation (Oman)—how authigenic carbonate changes a global pattern. The Depositional Record 2(1): 97–117

Yose LA, Strohmenger CJ, Al-Hosani I, Bloch G, Al-Mehairi Y (2010) Sequence stratigraphic evolution of an Aptian carbonate platform (Shu'aiba Formation), eastern Arabian plate, onshore Abu Dhabi, United Arab Emirates. In van Buchem FSP, Al-Husseini MI, Maurer F, Droste HJ (eds) Barremian–Aptian stratigraphy and hydrocarbon habitat of the eastern Arabian plate. Geoarabia Spec Pub 4(2):309–340

Zakhera MS (2010) Cenomanian-Turonian rudists from western Sinai, Egypt systematic paleontology and paleoecology. Geobios 44: 409–433

Zeebe RE (2001) Seawater pH and isotopic paleotemperatures of Cretaceous oceans. Palaeogeogr Palaeoclimatol Palaeoecol 170: 49–57

Zheng X, Jenkyns HC, Gale AS, Ward DG, Henderson GM (2013) Changing ocean circulation and hydrothermal inputs during ocean anoxic event 2 (Cenomanian–Turonian): evidence from Nd-isotopes in the European shelf sea. Earth Planet Sci Lett 375:338–348

Zheng X, Jenkyns HC, Gale AS, Ward DG, Henderson GM (2016) A climatic control on reorganization of ocean circulation during the mid-Cenomanian event and Cenomanian-Turonian oceanic anoxic event (OAE2): nd isotope evidence. Geology 44:151–154

Ziko A, Darwish M, Eweda S (1993) Late Cretaceous-Early Tertiary stratigraphy of the themed area, east central Sinai, Egypt. N Jb Geol Palaeont Mh, H 3:135–149